uOttawa

L'Université canadienne
Canada's university

FACULTÉ DES ÉTUDES SUPÉRIEURES ET POSTOCTORALES

u Ottawa

L'Université canadienne
Canada's university

FACULTY OF GRADUATE AND POSDOCTORAL STUDIES

Dominique Renée Dugay
AUTEUR DE LA THÈSE / AUTHOR OF THESIS

M.Sc. (Chemistry)
GRADE / DEGREE

Department of Chemistry
FACULTÉ, ÉCOLE, DÉPARTEMENT / FACULTY, SCHOOL, DEPARTMENT

Cellular Imaging Through Functionalized Carborane-Containing Silver Nanoparticles Utilizing Surface Enhanced Raman Scattering Spectroscopy

TITRE DE LA THÈSE / TITLE OF THESIS

Darrin Richeson
DIRECTEUR (DIRECTRICE) DE LA THÈSE / THESIS SUPERVISOR

CO-DIRECTEUR (CO-DIRECTRICE) DE LA THÈSE / THESIS CO-SUPERVISOR

Tom Baker

John Pezacki

Gary W. Slater
Le Doyen de la Faculté des études supérieures et postdoctorales / Dean of the Faculty of Graduate and Postdoctoral Studies

Cellular Imaging through Functionalized Carborane-Containing Silver Nanoparticles Utilizing Surface Enhanced Raman Scattering Spectroscopy

Dominique R. Duguay

A thesis submitted to the Faculty of Graduate and Postdoctoral Studies

in partial fulfillment of the requirements for the degree of

Master of Science

in the Ottawa-Carleton Chemistry Institute

Department of Chemistry, University of Ottawa

uOttawa

L'Université canadienne
Canada's university

Université d'Ottawa • University of Ottawa

Candidate

Dominique R. Duguay

Supervisor

Professor D. S. Richeson

Your file Votre référence
ISBN: 978-0-494-65512-2
Our file Notre référence
ISBN: 978-0-494-65512-2

Acknowledgements

Who ever thought while delaying the inevitable real world for 2 years I would have met such amazing people? I would like to take this opportunity to thank all the people in my life who have made my life at UOttawa great! Nat, our chief lab leader and my early morning associate (I actually like mornings now, thanks!); Ian I-Dawg Mallov, a hard worker, great friend, and hardcore party animal; Jess, who loves music, socializing, and market shopping (I love doing these things with you!). We four started out as the group core, and it made moving to Ottawa so much easier! Titel and Ahmed, both desk neighbours and later additions, we aren't complete without your antics. I'd also like to thank all my other friends at the university and beyond, for making the past two years great and entertaining! Mark Perry (the first non-lab member I met), James, Becky, Cory, Chris, Steve, Lisa, Andre, Joel, Terri, and of course Adrian. It wouldn't have been fun without you guys.

As for family support, I have lots! Thanks to my mom and Doug, trekking all the way up here for business, but bringing me tokens from home (Belliveau wine anyone?). Thanks to Erica, my wonderful artsy sister whom sometimes I get along with a lot better long-distantly (we'll work on that), and Daddy, for being a phone call away (and for all the fantastic food, and helping me finally past my driver's test!). I'd like to thank all my extended family who always had my back, and inspired me through their struggles to complete research that matters. I love being at Square Lake with everyone, it makes my summer.

I would like to thank my supervisor Darrin, for being supportive and always having new ideas (especially when the old ones aren't working). My collaborators, David Kennedy and John Pezacki, thank you for all the hard work that went into this project.

Lastly, thanks are extended to the Canadian Institutes of Health Research, as well as Natural Sciences and Engineering Research Council of Canada, and University of Ottawa, for all their financial support and making this project possible.

Contents

List of Figures

List of Tables

List of Schemes

List of Abbreviations

Å	angstrom unit, 10^{-10} m
Ar	aromatic group
Bu	butyl (^{t}Bu, *tertiary*-butyl)
Bn	benzyl
BNCT	Boron Neutron Capture Therapy
Cp	cyclopentadienyl, C_5Me_5
δ	chemical shift in ppm
d	doublet
DME	dimethoxyethane
DCM	dichloromethane
Et	ethyl
^{i}Pr	*iso*-propyl
IR	infrared
m	multiplet
M	moles per litre, or metal in a reaction scheme
Me	methyl
NMR	nuclear magnetic resonance
Ph	phenyl
ppm	parts per million
R	alkyl or aryl group
s	singlet
SEM	Scanning Electron Microscope
SERS	Surface Enhanced Raman Scattering
t	triplet
THF	tetrahydrofuran
X	halogen

Abstract

This thesis focuses on various carborane compounds and their uses for targeted cellular imaging. Cellular imaging agents have been developed for the field of medical diagnosis and treatment for some time. Many different processes have been traditionally applied in these fields, including fluorescence tagging, but these are lacking in differentiation from cellular background signals. Herein, carborane compounds have been developed for use as Raman reporters with signature absorption for BH vibrations, inside of the cell silence vibrational range. Carboranes have also been studied for the application of Boron Neutron Capture Therapy, a binary radiation therapy technique. Coupling these two ideas has lead to the formation of specific cellular targeting agents utilizing the unique BH vibrations for imaging, as well as the possible application of BNCT to the malignant tissue. This process has been developed with the aid of silver nanoparticles, which have been shown to enhance the Raman signal up to a factor of 10^{14} with Surface Enhanced Raman Scattering (SERS) techniques. Functionalized carborane compounds have been developed in order to study BH vibrations, and carborane-containing functionalized silver nanoparticles have been applied to target anti-EGFR antibodies for malignant tissue detection. Resulting SERS images confirmed selective tissue targeting with nanoparticle aggregate hot spots. Overlaying scanning electron microscope images with SERS BH vibrational intensity maps provided additional information on concentrations of cell surface receptors and identifying intercellular structures. Elaboration of the carborane Raman reporter resulted in two other carboranes with key functional groups, which could increase solubility, and have additional Raman handles for identification.

Chapter 1

Nanoparticles, Imaging, and SERS

Introduction

Fluorescence can be applied in a variety of ways for tracking and analyzing biological molecules; general methods for imaging are intrinsic and extrinsic fluorescence. Intrinsic fluorescence, which draws on naturally present features in the molecule, can be applied by utilizing autofluorescent molecules like tryptophan, NADH, or the recently discovered green fluorescent protein associated with the Nobel Prize in Chemistry in 2008. Extrinsic fluorescence occurs once a cellular component, such as proteins, nucleic acids, or lipids are labelled with a fluorophore. The easiest way to attach a fluorophore is through reactions with amino groups, thiols, carboxyl groups, or azides. Fluorophores themselves are fluorescent dyes which have molecular components that can absorb light of one frequency and reemit it at another. For example, many of these compounds contain an aromatic functionality, which stabilizes absorbed energy. Such groups commonly absorb light when π electrons are excited to higher energy π^* levels. Quantum dots can also be used, which are composed of semiconducting colloids like cadmium selenide and sulfide, as well as indium phosphide and arsenide. These species absorb light that corresponds to the band gap of the particular material.

Fluorescence is one form of luminescence, the other two being phosphorescence and chemiluminescence. Fluorescence occurs when one or more electrons absorb a photon and are excited to a higher electronic energy level. The excited electron occupies various vibrational levels within the excited electronic state and will rapidly relax to the

lowest vibrational level. Once the electrons decay to the ground state, over the period of 10^{-9} seconds[1], they emit energy in the form of a photon with a larger wavelength. The difference between the energies of the photons emitted is defined as the Stokes' Shift. A variation of fluorescence, called delayed fluorescence, occurs when the electron falls through "intersystem crossing" to a triplet state, reverts back to the lowest excited singlet state, and then finally falls to the ground state with photon emission, which takes approximately 10^{-6} seconds.[1] The intersystem crossing involves a change in spin multiplicity and is a formally forbidden transition.

These energy transitions can be summarized using a Jablonski Diagram as shown in Figure 1.1.

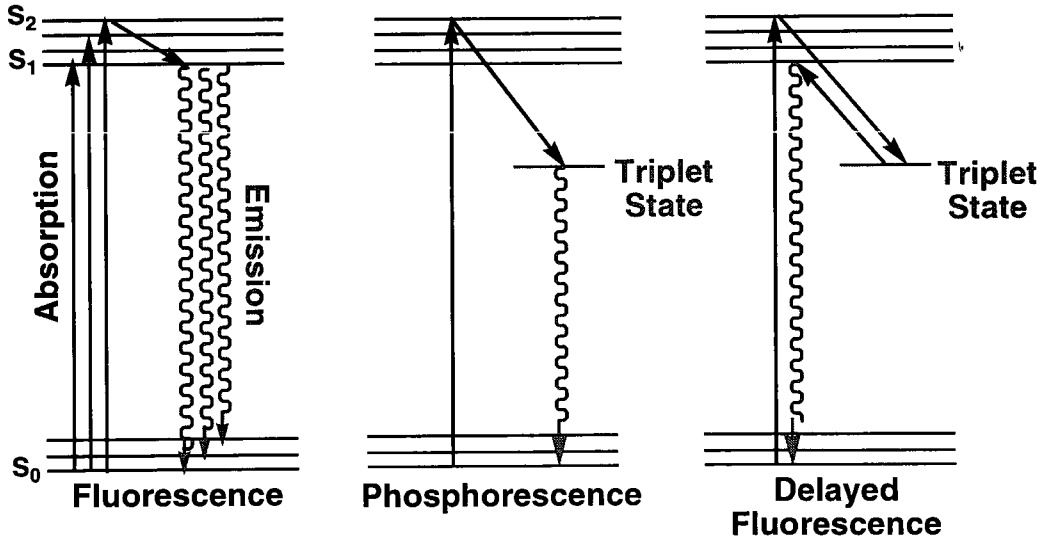

Figure 1.1: Jablonski Diagram of energy absorption and emission

While fluorescence imaging has a long and illustrious history, one can imagine other spectroscopic methods being applied to imaging. Rather than the electronic transitions employed in fluorescence and fluorescent dye imaging, vibrational transition could be utilized as the method to monitor or image a molecular species. However, a limitation on vibrational imaging would be the presence of interfering vibrations from the background matrix. In the case of cellular targets this would correspond to a plethora of organic components of the cell and its surroundings. On the other hand, there is a "silent region" for cellular and common organic species, in the range of approximately 1800-2100 cm^{-1} (IR). If a probe were designed so as to have a characteristic vibration in this region, it would have potential application as a vibrational imaging agent. Vibrational imaging would allow application of either FT-IR or Raman vibrational spectroscopy

Raman and FT-IR spectroscopy are easily applied techniques, since many vibrationally active functional groups can be integrated into the targeted system. A method that employs organometallic tracers for biological studies, carbonylmetallo immunoassay (CMIA), utilizes bands that appear in the region of 1900-2100 cm^{-1} through FT-IR. Transition metal complexes, such as $Cr(CO)_3$, $Mo_2Cp_2(CO)_4$ ($Cp = \eta^5$-C_5H_5), $Mn(CO)_3$, and $Co_2(CO)_6$, interact with peptides and proteins through activated carboxylic acids, and have a detection limit in the picomole range.[2] Since the carbonyl group is coordinated to a transition metal center, it has a significant shift from common organic bonds due to the electron deficiency of metal. Current research is pursuing the integration of these organometallic complexes to antibodies and pharmaceuticals for imaging.

Infrared spectroscopy uses the elasticity of bonds in the mid-infrared region (400-4000 cm^{-1}) to study the vibrational motions which occur when an IR beam is passed through the sample. These vibrations (stretching, scissoring, wagging, rocking, and twisting) occur at specific wavelengths for certain organic covalent bonds, which allows for simple diagnostic bands. Figure 1.2 presents the spectral regions for common organic functionalities. It is very clear that a vacancy of stretching for common organic materials occurs from 1800-2100 cm^{-1} and 2400-2800 cm^{-1}, which can be utilised for various target imaging.

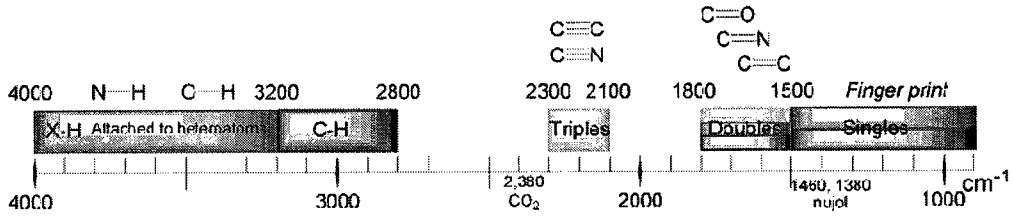

Figure 1.2: IR Spectroscopic Summary of Bond Absorption[3]

Raman spectroscopy was discovered in 1928 by Sir C.V. Raman, who was awarded a Nobel Prize in Physics in 1930 for its discovery. Raman spectroscopy relies on the inelasticity of bonds, which is complementary to IR spectroscopic information. In IR spectroscopy, the energy beam has a range of frequencies, of which specific frequencies match vibrational excited states. Raman spectroscopy only uses one frequency to irradiate the sample, and the radiation then scatters from the molecule; the changes in the incident energy are measured (ΔE). When the energy beam irradiates the sample, it polarizes the electron cloud to a higher energy state. The energy from the light wave is transferred to the polarized molecule for a very short life time where it forms a "complex". The "complex" is so unstable that it instantly scatters the energy and falls from the virtual

state to the vibrational states. This whole process is so fast that the nuclei of the molecule stay in a distorted electron arrangement without reaching a new equilibrium. The energy that is scattered from the molecule is classified as Rayleigh or Raman scattering. Rayleigh scattering is elastic; only electron cloud distortion is involved, and relaxation occurs without nuclear movement or changes in energy. Raman scattering is inelastic, where nuclear motion is triggered by the light interaction. This process involves a change in energy, transferred from the incident photon to the molecule, or from the molecule to the scattered photon. This causes a difference in energy by one vibrational unit, and it will only happen once every 10^7 photons scatter. Raman scattering can further be divided into Stokes' scattering and Anti-Stokes' scattering. Stokes' scattering begins when the molecule is in the ground state, and Anti-Stokes' scattering begins in the excited state (Figure 1.3). Stokes' scattering is more prominent since most molecules are at the ground state prior to excitation; the ratio of Stokes' to Anti-Stokes' scattering can be calculated from the Boltzmann equation.

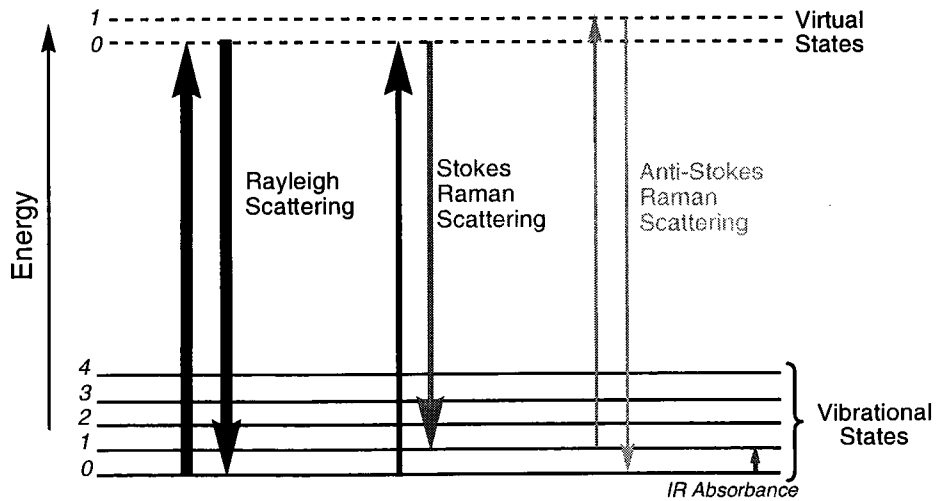

Figure 1.3: Scattering process where energies are larger than vibrational states

The polarization of the electron cloud is stronger for symmetrical molecules than for unsymmetrical molecules (for which IR is stronger). For this reason, molecules like C=N, N_2, and O_2 have strong Raman signals. Other polyatomic compounds may display multiple peaks, called a fingerprint, which can have both Raman and IR active vibrations. With organic and inorganic compounds, symmetry elements and point groups can determine whether the vibration will be IR active, Raman active, or both. This is illustrated with CO_2 in Figure 1.4.

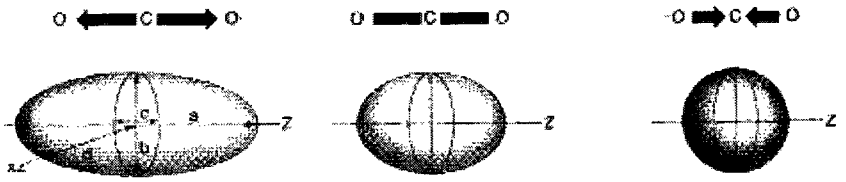

Figure 1.4: Example of CO_2 Polarization of Ellipsoid[4]

With new discoveries and evolving theories, spectroscopic methods and their potential applications are developing to improve sensitivity, enhancement, and ultimately will lead to single molecule detection. In 1974, a group lead by Fleischman discovered an enormous enhancement of a factor of 10^6 of the Raman scattering from an aqueous pyridine solution that adsorbed onto a roughened silver electrode. They deemed this enhancement was due to an increase in electrode surface area. Two other groups studied the enhanced intensity, and in 1977 they concluded that increased surface area would only account for a factor of 10, not 10^6 as recorded. These studies lead to two different theories for large increases in intensity. Jeanmarie and Van Duyne proposed the

electromagnetic theory, and Albrecht and Creighton proposed the chemical (or charge-transfer) theory. Both theories still hold today, although now the competition has modified into coordinating explanations. It was generally accepted that the electromagnetic theory accounts for 10^4 times the enhancement over traditional Raman, while charge transfer theory accounts for a factor of 10^2.[5] The electromagnetic theory, which is most often cited, occurs when an analyte is adsorbed onto a metal surface, and the metal conduction electrons are excited by a light beam, which oscillate as a collective group across the metal surface. These oscillations are called surface plasmon resonances (SPR). The electron density extends considerably from the metal surface, since the metal centers are positively charged. This results in free lateral flowing electron density, and once excited, surface plasmon resonance. As with most spectroscopic surfaces, there are certain resonance frequencies which scatter most effectively. With silver and gold nanoparticles, the plasmons resonate in the visible region, which is easily coordinated with visible and NIR lasers utilized in Raman scattering. Other metals have also been applied, including copper, and to a lesser extent platinum and palladium.[6] The scattering only arises when oscillations are perpendicular to the surface plane, in roughened valleys. When plasmons move up to the peak of the metal surface and scatter they are sometimes called lightning rods. If the metal surface is smooth, only absorption can occur. This effect is demonstrated in Figure 1.5. Evidence supporting the two theories includes the notion that EM enhancement should be non-selective; all Raman scattering for adsorbed molecules should be amplified by the same factor, provided the surface is the same. However, CO and N_2 adsorbed molecules vary by a factor of 200 for SERS intensities,

even with constant experimental conditions. This increase in intensities is explained with charge transfer theory.

The chemical theory (or charge transfer theory) arises from the analyte chemically bonding to the surface through its valence electrons. When the light beam causes

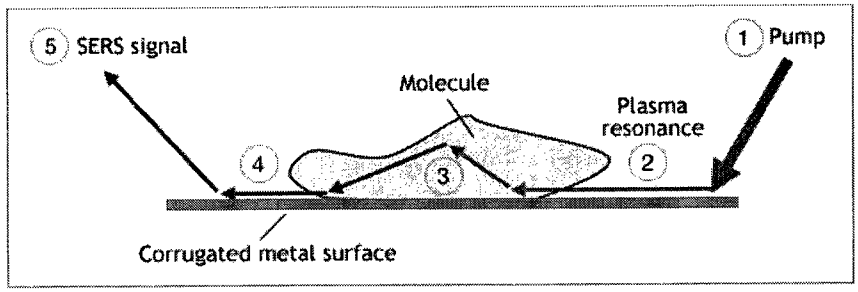

Figure 1.5: SERS process steps: 1) light beam irradiates metal surface 2) plasmon excitation 3) energy is scattered by the molecule 4) Raman scattered light is transferred back to the plasmons 5) Raman scattered light is emitted to form SERS signal.[7]

excitations, the electrons transfer from the metal to the molecule, and back to the metal. It is plain to see this is a different interaction versus the electromagnetic enhancement, where the interaction is between the analyte and the plasmons. The charge transfer effect can either go from metal to molecule or the opposite direction, depending on the HOMO and LUMO levels of the molecule, and the Fermi levels of the metal. The adsorbed analytes with low lying unfilled π orbitals, like pyridine, have charge transfers from metal to molecule. Meanwhile, analytes like NH_3 and piperidine undergo charge transfers from molecule to metal, since the π orbitals are filled.[8] The enhancement arises from new electronic states from chemisorption, which function as resonant intermediate states for

Raman scattering.[9] The Raman scattering produced by charge transfer for an ethylene molecule can be represented by:

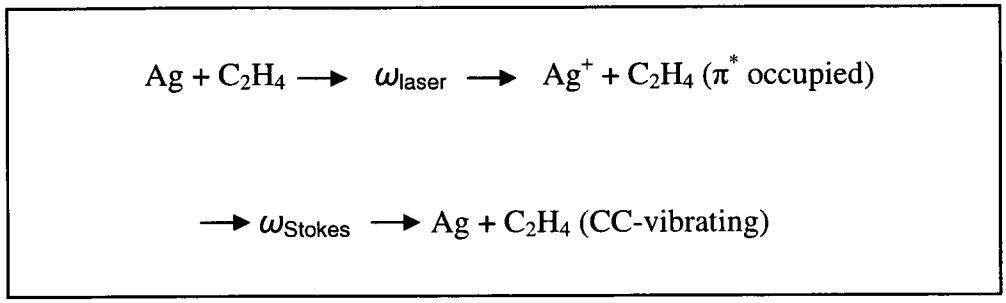

Scheme 1.1: The charge transfer of an ethylene molecule, which produces Raman Scattering.[10]

There exists a third contribution to the Raman scattering enhancement, and it is based on the observation that adsorbed molecules which have internal resonances can boost Raman intensities. This newer theory on the contribution of the adsorbed compound is particularly important for experiments involving very small quantities; these can result in very large enhancements and even single molecule observations. Until recently, the three theories were predominantly treated separately, and had more of a coincidental contribution when analyzing the overall effect. This is because of so many variables within a SERS experiment; it's hard to pinpoint what scattering is due to which theory effect. To decipher the enhancement source, experiments with large ranges of wavelengths would be required, especially to study all of the different ranges of excitations. However, Raman experiments only involve one or a few excitation wavelength, so the experiments would prove to be costly and time consuming.[8]

Another factor contributing to enhancement is the clustering of silver colloids. Both Metiu and Nitzan explored this concept in the early 1980's, and saw that at the proper wavelength and polarization and small interparticle gap they could see Raman enhancements on the magnitude of 10^{10}.[11] More recently, research has been conducted where 10^{11} enhancements are possible when two nanoparticles are brought closer than one nanometre from each other.[12] The enhancement rapidly decreases with increasing interparticle gap. The rationalization for this coupling comes from the increase in polarization by the two nanoparticles. The mutual interaction between the nanoparticles increases the induced dipole, and produces a large field felt by the adsorbed molecules. The field produced by incident light contributes to the induced dipole, as the field of the neighbouring nanoparticle affects its partner as well. These increases in Raman scattering enhancements can produce hot spots (Fig 1.6), which are easily visible and are made up

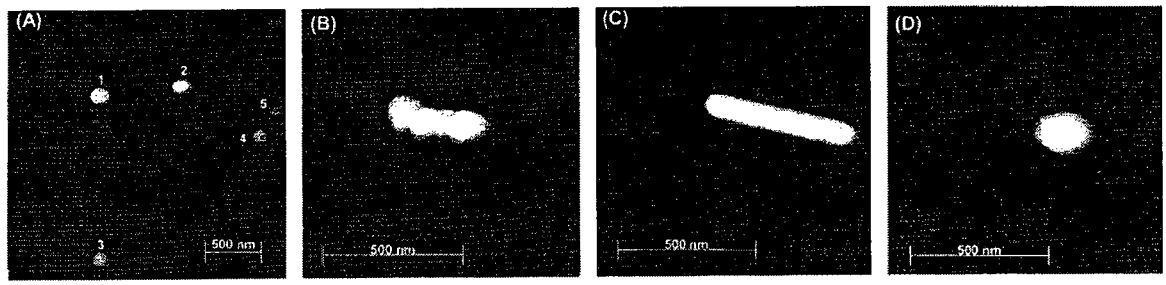

Figure 1.6: Atomic force microscopy images of silver nanoparticles. A) NP 1 and 2 hot spots, others are not. B) Four particle aggregate hot spot. C) Hot nanorod D) Faceted hot particle.[13]

of coupling of only a few nanoparticles. The final spectrum resulting from SERS is not necessarily an enhanced version of the Raman counterpart. Band intensities decrease with increasing vibrational frequencies. This means stretches like C-H are weaker in SERS than would be commonly expected. However, the extremely large increases in Raman scattering for other frequencies make the SERS method a worth while effort.

Although fluorescent dyes have been the common labelling technique for some decades, recent advances in metal nanostructure biotechnology have begun to eclipse them in application. These metal nanostructures have significant enhancements in both optical and photothermal properties, which will be further discussed below. Nanostructures, including nanoparticles, nanorods, and quantum dots, demonstrate strong scattering and absorptions when in the presence of light. Nanoparticle colloids have unique interactions with light which result in bright and intense colours of gold, red, and purple, depending on the nanoparticle diametre. As previously discussed, the enhanced scattering from nanostructures is defined as localized surface plasmon resonance (LSPR); the oscillating electromagnetic field of light irradiates the free electrons from the metal, resulting in a collective coherent oscillation of the electrons. These resulting oscillating electrons are known as "plasmons", and form a conductive band at ~ 100 nm for gold nanoparticles.[14] This explanation can be simplified as "a photon confined to the small size of the nanostructure, constituting an intense electric field around the particle".[15] The metals most commonly utilized for nanostructure capabilities - gold, silver, and copper - also have other therapeutic properties. Gold has long been used as an agent for anti-inflammatory therapy, including many applications in arthritis. Silver, on the other hand, has been used as an antibacterial agent in low doses. Amazingly, silver compounds for

the fight against bacteria have been popping up in commercial capacities, available off the shelf.[16] Copper oxidises easily, so silver and gold are more applicable for optical imaging. Recently, research has been conducted exploring the use of silver nanoparticles as a bactericide. One research group concluded that the nanoparticles act in three different ways against certain bacterium. First, nanoparticles in the range of 1-10 nm attach to the surface of the cell membrane, which disrupts cellular functions like respiration and permeability. Second, the nanoparticles enter the bacterium and interact with compounds containing sulfur and phosphorus, causing damage to functions like DNA. Third, the nanoparticles release silver ions, which have traditionally been bactericidal agents and can inactivate enzymes through interactions with thiol groups.[17] These conclusions show the wide range of capabilities of silver nanoparticles, from Raman scattering enhancements to bactericidal compound.

Figure 1.7: Silver Shield, distributed by Nature's Sunshine®, is sold as a liquid or gel, with concentrations of 18-24 ppm of silver colloid.[16]

For the application of SERS, the hierarchy of enhancement from the metal centers begins with silver and alkali metals, which exhibit the most scattering. Next are gold, and then copper, followed by good conductors like aluminum, indium, and platinum. Transition metals are last and would not show much enhancement since they are poor conductors. Overall, silver and gold are most often used because their plasmons resonate in the visible region. Once the nanoparticle is irradiated and the conduction electrons are excited, the resulting LSPR decays and this release of energy can lead to light scattering, or nonradiative decay. The nonradiative process converts light to heat.[18] At the specific

LSPR frequency, a few things occur. The electric field intensity and both the scattering and absorption cross-sections are enhanced quite impressively in the visible region.[19]

The different nanostructures available have varying abilities, and can be tuned for several applications. Nanorods have two plasmon bands instead of one, and these display a band in the visible region (described above) and another band in the near IR region. These band frequencies are tuneable, and they depend on the transverse and longitudinal axis of the nanorods and their ratios to one another (see Figure 1.8).[14,20] Nanoparticles are spherical and are produced by reduction of metal salts. Most nanoparticles employed in

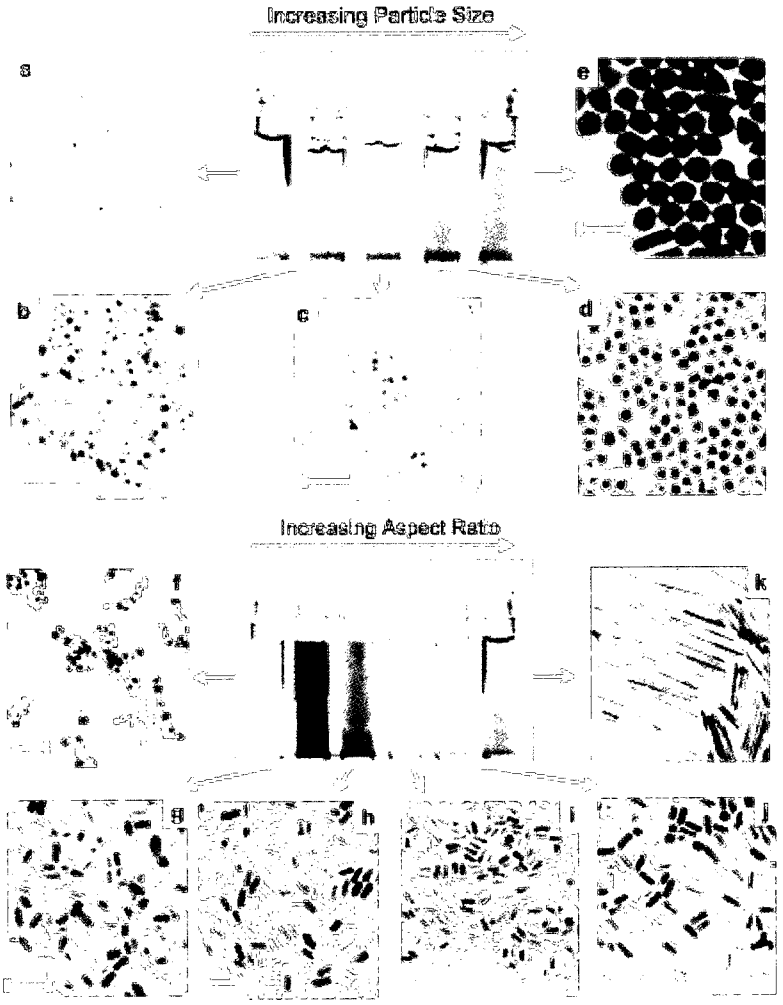

Figure 1.8: Aqueous solution photograph of gold nanoparticles (above) and gold nanorods (below). Variance in colour is due to different plasmon bands sensitivity to size. TEM images scale bars = 100 nm. Spheres a-e vary from 4 to 40 nm. Rods f-j have aspect ratios varying from 1.3 to 5, and 20 for k.[14]

both imaging and absorption range from 10 to 100 nm in diameter. Gold and silver nanoparticles have such high scattering properties, each nanoparticle as an optical probe is equivalent to a million dye molecules.[21] Nanoparticles are also more favourable for cellular imaging since they do not undergo photobleaching like fluorescent dyes, which results in higher attainable energies.[22] Nanoparticles can also be tuned to suit the specific application, and can be integrated into biological systems since they are on the same size scale.[23] Spherical nanoparticles with silica cores, known as silica nanospheres or nanoshells, can be tuned by decreasing the metal coated shell thickness, which will shift the LSPR from visible to NIR regions.[24]

Nanoshells have been examined in therapeutic applications involving the absorption of NIR energy, which causes localized heat sources. These localized heat sources can destroy cells; this process is called thermal tumour ablation. Nanoshells have been shown to have absorption cross sections of NIR energy 6 orders of magnitude greater than indocyanine green dye. Some other techniques of thermal therapy include laser light heat sources[25], focused ultrasounds[26], and microwaves[27]. However, these simple processes cannot distinguish between normal and malignant tissue, and treatment of imbedded tumours would have to involve penetration of healthy tissue. Functionalized nanoshells have been developed to target malignant tissue, and with the peak optical absorbance tuned to the optimal NIR region, the surrounding healthy tissue is not affected. This method was tested on mice[28], where tumours were grown to the size of 5.5mm. The mice were treated with targeted gold nanoshells, and the tumours were then illuminated with a diode laser. The results were quite notable; all mice which had treated tumours recovered and were tumour free even 90 days later. All mice in control groups,

which did not receive nanoshell solution injections, had to be euthanized 9-12 days post treatment since the tumours grew in excess of 10 mm. The laser was also focused to areas surrounding the tissue, but this did not destroy any cells; the nanoshells were properly targeted to the cancerous cells.[27]

This small survey of imaging techniques and applications demonstrates why it is important to further investigate imaging and therapies with these concepts. SERS, Raman spectroscopy, and the application of thermal therapy will be further investigated in the coming chapters. The Raman reporter utilized in our research, carborane, and its other medical applications will be introduced in the next chapter.

Chapter 2

Carborane

2.1 Introduction

Dicarba-*closo*-dodecaborane, most commonly known as carbaborane (IUPAC) or carborane, is a boron rich cluster compound comprised of 10 boron, two carbon, and 12 hydrogen atoms, $C_2B_{10}H_{12}$. Carborane exists as three isomers, *ortho (o)*, *meta (m)*, and *para (p)*, depending on the positions of the carbon atoms. When the carbon atoms are in positions 1 and 2, they are considered *ortho* carbons. Similarly, *meta* carbons are in positions 1 and 7, and *para* in positions 1 and 12. The carborane positions are identified in Figure 2.1. These clusters have an icosahedral geometry, where carbon and boron atoms are hexacoordinate. The IUPAC numbering of the atom positions is commonly referred to for the reactivity of the centers.

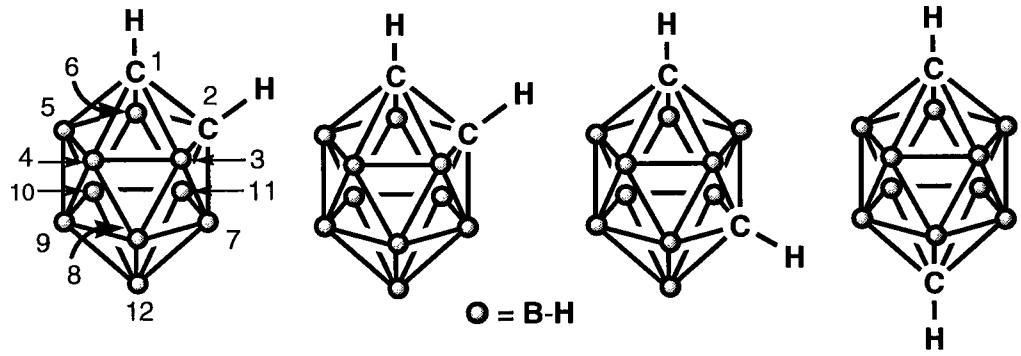

Figure 2.1: IUPAC Numbering Scheme, *ortho*, *meta*, and *para*-carborane

Carborane can be synthesized by reacting decaborane with an alkyne (mono and disubstituted) with a weak Lewis base catalyst as summarized in Scheme 2.1. The

shorthand notation of o-carborane is a triangle with two carbons and a $B_{10}H_{10}$ group, with a circle in the center denoting pseudoaromaticity. The first carborane synthesis was that of *o*-carborane, produced in 1963 by two independent groups.[29] Typical Lewis base catalysts include acetonitrile, alkyl sulfides, and alkylamines.[30] These generate the $B_{10}H_{12}L_2$ moiety upon reaction with decaborane, in which the acetylene undergoes a subsequent reaction to form the target product. These reactions are typically preformed in inert atmospheres, and are heated to reflux for several hours. One of the fascinating aspects of this synthesis is the variability of the acetylene employed. The acetylenes can have ether, carbamate, halide, ester, and nitro group functionalities. On the other hand, the acetylene cannot have nucleophilic species such as amines, alcohols, or acids for the reaction to proceed. This reaction has an average yield of 40 to 60%, and is the precursor for *meta* and *para*-carborane.

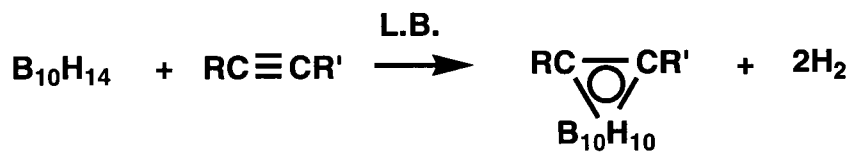

Scheme 2.1: Synthesis of *o*-carborane

This initially formed *o*-carborane is remarkably stable, and exhibits a high thermal stability up to 400°C. Further heating will rearrange the cage structure to the *meta* isomer (between 400 and 500°C) following a triangular face rotation mechanism,[31] and *m*-carborane subsequently rearranges to *para*-carborane (between 600 and 700°C) through a

pseudo "nido" state.[32] These properties are drastically different from the starting decaborane, which has a melting point of 98°C and a decomposition point at 170° C.[33]

Carborane reactivity is dependent on the isomer in question. For example, the CH group on *o*-carborane is more acidic than that in the meta or para isomers. The acidity depends on the neighbouring CH distance, as carbon has a greater electronegativity compared to all other boron vertices. The CH groups have the following relative acidities: pK_a *ortho* = 22.0, pK_a *meta*= 25.6, pK_a *para*=26.8.[34] This enables general reactions to be conducted by deprotonation with a strong base (alkyl lithium) producing a reactive nucleophile, which can further react with halogens, alkyl halides, carbon dioxide, and aldehydes. Most favourable reactions involve relatively unhindered reagents since the carborane cage is bulky. With *o*-carborane reactions, looks can be deceiving, since there is equilibrium with the protonated and dianion forms (Scheme 2.2). This disproportionation hinders many reaction outcomes when attempting a single CH functionalization.

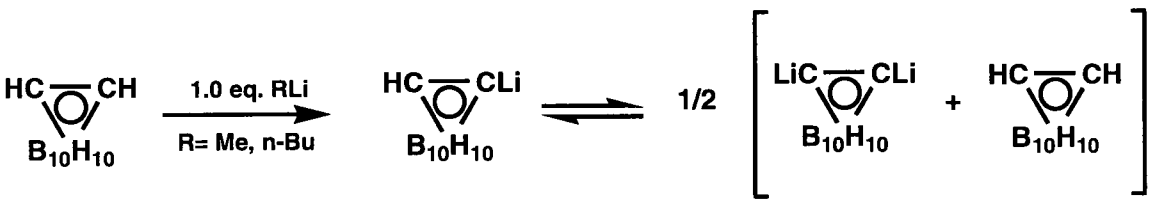

Scheme 2.2: *o*-carborane disproportionation

Reactions can also occur on the BH vertices. These functionalizations are produced by direct electrophilic halogenations[32], sulfhydration[35], alkylation[32,36], and metalation.[37] Once a vertex has been functionalized, the normal reactivity of all other

vertices can be affected. This, along with its increased thermal stability, renders carborane as a pseudoaromatic compound.

There are many different methods of characterizing carborane compounds. Nuclear Magnetic Resonance (NMR) is easily applicable, with both ^{1}H and ^{11}B spin active nuclei relatively abundant. Boron has two spin active isotopes; ^{11}B has a spin of 3/2 and is 80.42% abundant, while ^{10}B has a spin of 3 and is 19.58% abundant. The boron signal will always be broadened due to the fact that both of the isotopes are quadrupolar. Most often ^{11}B NMR is conducted, since the nuclei is more abundant and has better sensitivity, unless ^{10}B is desired for neutron capture therapy purposes. One of the drawbacks to boron NMR is the presence of borosilicate from the NMR tubes. To produce a clear signal, very concentrated samples must be used. Other alternative methods include purchasing boron-free tubes, or applying a spin-echo pulse sequence in an effort to remove background noise.[38] Proton NMR is very useful in characterizing carborane compounds, once decoupled from ^{11}B. The resultant signal will still be slightly broadened due to coupling with ^{10}B, but it will still produce a diagnostic spectrum, as illustrated in Figure 2.2.

Other diagnostic methods include TLC, X-ray crystallography, HPLC, and IR. These methods are often employed to map the progress of a reaction, not to solely characterize a compound. The BH signal resulting from the IR spectra is fairly strong, due to having 10 BH vertices in the carborane cluster. The BH stretching frequency appears at 2600 cm^{-1}, with the CH frequency emerging at 3079 cm^{-1} (ortho), 3070 cm^{-1} (meta), and 3065 cm^{-1} (para).

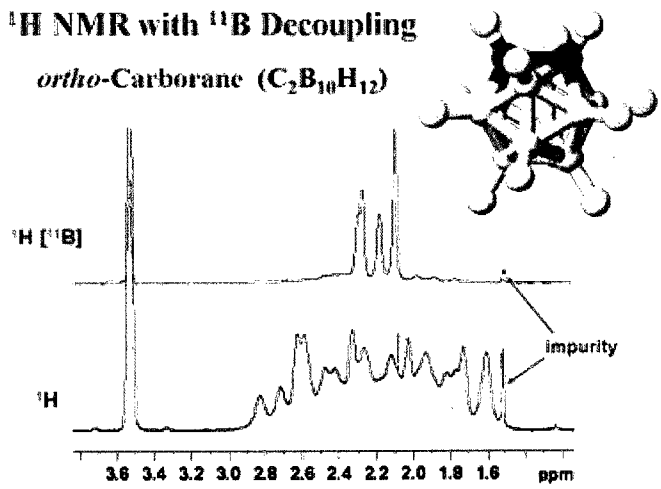

Figure 2.2: *o*-carborane ^{1}H and ^{1}H{^{11}B} NMR Spectra demonstrating the huge amount of coupling between ^{1}H and ^{11}B nuclei[39]

Carboranes can be applied in many different ways for medicinal purposes, including imaging, as well as therapeutic applications. One of the most sought after applications is Boron Neutron Capture therapy, a binary therapy, which was amazingly first considered in 1936 by Locher.[40] This process involves the inclusion of a high concentration of ^{10}B atoms, which is easily obtained from the 10 BH vertices of carborane. Boron-10 is irradiated by a beam of thermal neutrons, which produces ^{4}He alpha particles as well as ^{7}Li ions. The α-particle and the lithium ion only travel a distance of 12 microns[41], which is the average diameter of a cell. As a result, the energy released by this reaction is only deposited within a cell width; this can selectively destroy malignant cells. For the appropriate amount of energy to destroy the cell, it is estimated that between 10 and 30μg ^{10}B/g of tumour is required to be deposited, which can be

minimized based on localization near the nucleus.[42] Recently, carboranes have been researched for potential pharmaceutical and biological probe applications as well as BNCT. Carboranes can be utilized to increase hydrophobic interactions between medicinal agents and their targeted receptors. Carboranes can also increase the bioavailability of compounds, keeping them from being metabolized, thus increasing in vivo stability. Therefore, many research groups are now incorporating carborane as a

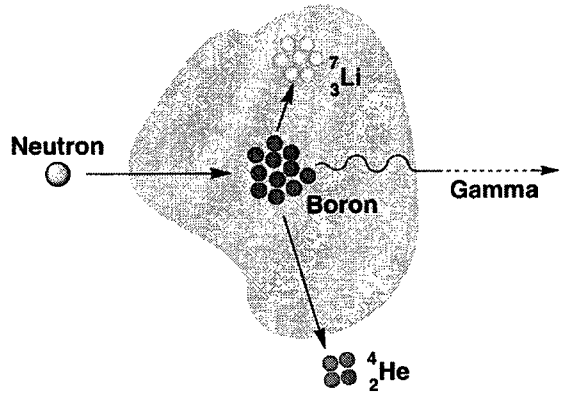

Figure 2.3: Illustration of Boron Neutron Capture Therapy[43]

pendant group, or synthon, when engineering new pharmaceutical paths. Since carborane is approximately the size of a 3D swept benzene ring, it can be easily incorporated in similar locations. For example, a X-ray structure (Figure 2.4) solved by the Valliant group illustrates carborane's similar size to the phenyl group, where the carborane diametre is 5.25 Å and the phenyl diametre is 4.72 Å.[44] Since carborane has a range of applications in the realm of biomolecules, a short review of some recent impacts of carborane chemistry is provided. This includes studies with carbohydrates, intercalators,

estrogen agonists, radiopharmaceuticals, MRI, amino acids, and Boron Neutron Capture Synovectomy.

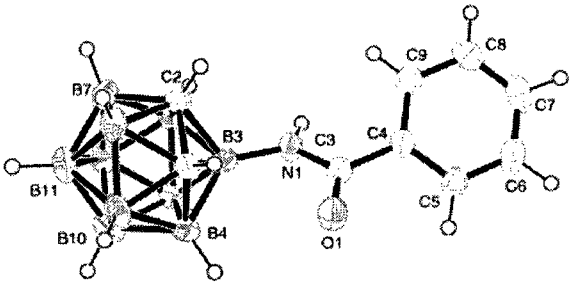

Figure 2.4: X-ray structure of 3-amino-*o*-carborane demonstrates carborane's similarity in size to the pendant phenyl group.[44]

Research involving carbohydrates has recently ameliorated due to advances in synthesis.[45] If using carborane as a BNCT agent, carbohydrates can function as the targeting device, since it binds to receptors specific to certain cancerous tumours. Carbohydrates can also limit the negative impact of the hydrophobicity of carboranes, which would be metabolized by the liver.[44] Recently, Tietze et al. have prepared carborane carbohydrate complexes which would target cancerous cells. This synthesis involved special alkynes prepared from sugars, and reaction between the new alkynes and decaborane in acetonitrile. From their library of compounds, maltoside (**1**) had the highest uptake in B16 melanoma cells and C6 rat glioma cells. These cells were irradiated with a dose of thermal neutrons and major cellular destruction was detected. The concentration of boron in the cells increased from 6.1 ppm in 3 hours to 20 ppm in 24 hours. The other compounds in the library included a lactoside (**2**) with maximum

boron concentration of 13.2 ppm at 12 hours and a glucoside (**3**) with maximum of boron of 11.2 ppm at 3 hours.[46] Various other studies were pursued to increase stability of the molecule by introducing side chains on the remaining CH of carborane.

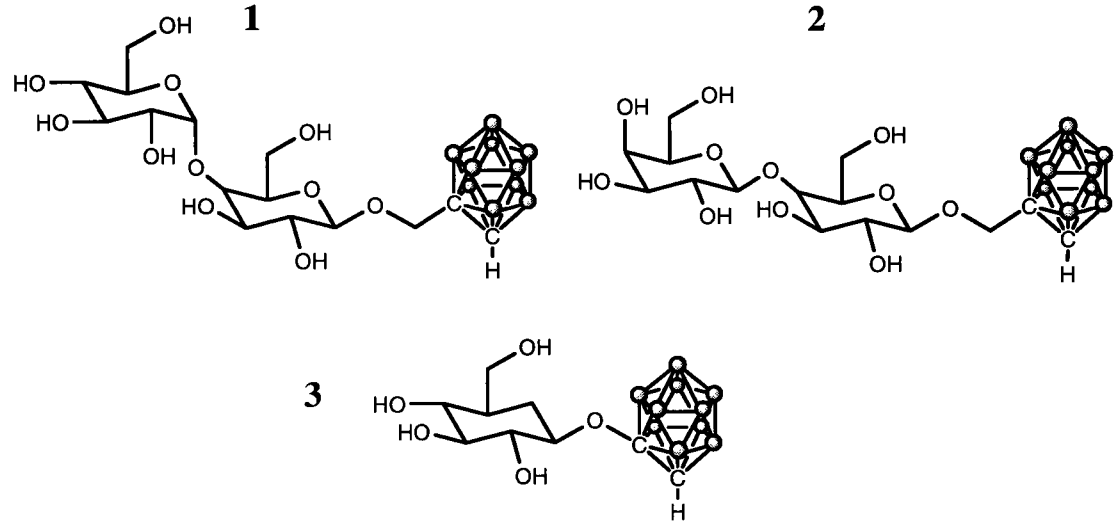

Figure 2.5: Carboranyl glycosides. (**1**) Maltoside, (**2**) Lactoside, and (**3**) Glucoside.[46]

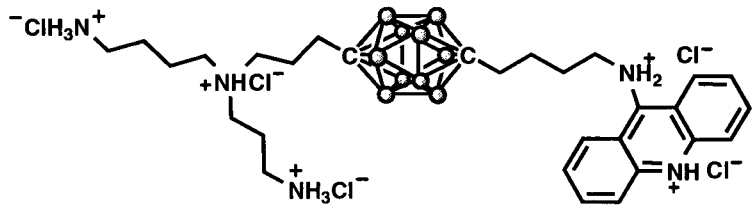

4

Figure 2.6: Intercalating hydrophilic compound (**4**).[48]

The integration of boron in near proximity to DNA is very important for BNCT. If carborane is placed closely to DNA, the amount of boron required for successful

therapy can be reduced.[47] A series of DNA intercalating compounds, composed of phenanthridine and acridine, were prepared with carborane by Gedda et al. These were analyzed with human glioma spheroid tissue.[48] The developed lipophilic compounds were cytotoxic and had poor penetration of the inner spheroid. The hydrophilic compounds had lower cytotoxicity and had improved accumulation in the cell, especially compound **4**. However, the accumulation of the carborane intercalators compounds is not target specific; tumour targeting agents need to be integrated into the system. Other biological moieties studied with carborane integration for the purpose of BNCT include liposomes[49], folic acids[50], and mitochondria[51]. These methods showed promising results with boron accumulation and are being investigated.

Amino acid containing carboranes have been developed and researched for a variety of properties. A carborane containing analogue of phenylalanine has been researched as a BNCT agent and a fungicide.[52] The fungicidal properties are very potent; it has over 1000 times more activity compared to a zoospore inhibitor fungicide used against *P. halstedii*.[53] Overall the *o*-carborane analogue was used for its hydrophobicity, but the other isomers are being researched as well.

Carborane has been applied as a pharmacore for research in neo-plastic and estrogen receptor areas. A pharmacore is a framework which is responsible for the drug's biological activity. These usually include steric and electronic features which interact with biological targets and trigger biological responses. Most pharmacores are hydrophobic, aromatic, hydrogen bond acceptor/donor, and a cation/anion.[54] A series of carborane containing salts, with carborane acting as a pharmacore, were tested for anti-neoplastic cytotoxic activity. The most active compound (**5**) greatly reduced DNA

synthesis by inhibiting regulatory enzymes involved with purine. This compound also inhibited the activity of nucleoside kinases, which affected deoxyribonucleotide clusters.[55] However, this compound does not specifically target DNA. Another carborane pharmacore study utilized carborane's hydrophobicity for estrogen receptor agonists. Estrogen receptor antagonists are used for treatments involving hormone dependent breast cancers. Here carborane was substituted in the C and D ring locations of 17β-estradiol. This location was chosen since the rings function by binding the steroid to the estrogen receptor though hydrophobic interactions. The requirements for the ring substitute include hydrophobic groups and H-bonding substituents to ensure sound

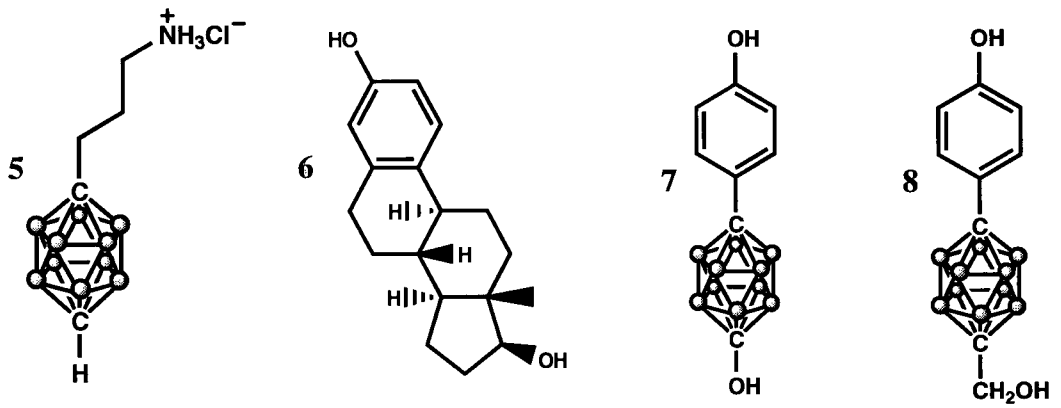

Figure 2.7: Pharmacore carborane compounds (**5**) amino-*o*-carborane hydrochloride, (**6**) 17β-estradiol, (**7**) and (**8**) 17β-estradiol derivatives where (**8**) has methylene spacer.[56]

estrogen receptor binding. A range of compounds was prepared by varying carborane isomer, OH groups, and pending groups from the CH moiety. From this analysis, it was concluded that the *para* isomer is more active than *meta*, and methylene spacers between carborane and alcohol substituents increase activity. However, methylene spacers greater

than n=1 negate the increased activity. Compounds **7** and **8** were actually more active than the original 17β-estradiol. Potency depended on the above variations, with **8** being 10 times more active than 17β-estradiol. Changing the phenol positions also affected activity, where 1, 4 positions were more favourable than 1, 3.[56] Overall the carborane compounds had high bonding affinities to the estrogen receptors, and a few research groups are pursuing further studies on the subject.[57]

Radiopharmaceuticals are another field being pursued with the integration of carborane. These are found in two categories, radiolabeled carboranes for the purpose of BNCT, or a core to construct a radiopharmaceutical. In some syntheses of transition metal complexes, carborane is used in the place of a cyclopentadienyl ring. One example includes a $[M(CO)_3]^+$ complex (M= Re, Tc^{99}), where carborane provides the remaining ligand framework for the metal center (Scheme 2.3).[58] Various different biomolecular applications of the $[M(CO)_3]^+$ complex are being researched by the Valliant group. The Hansen group reported the synthesis of a carborane functionalized-organic compound (**10**) for purposes of BNCT. Compound **10**, which was modeled after **9**, binds to minor groves found on DNA.[59] They also substituted ^{73}Se ($t_{1/2}$= 7.1 hrs) into the carborane compound framework for the purpose of tracking distribution by positron emission tomography (PET). This new compound (**11**) involved the substitution of ^{73}Se in the final step of synthesis by a reaction with cold Li_2Se with the ditosylate.[59]

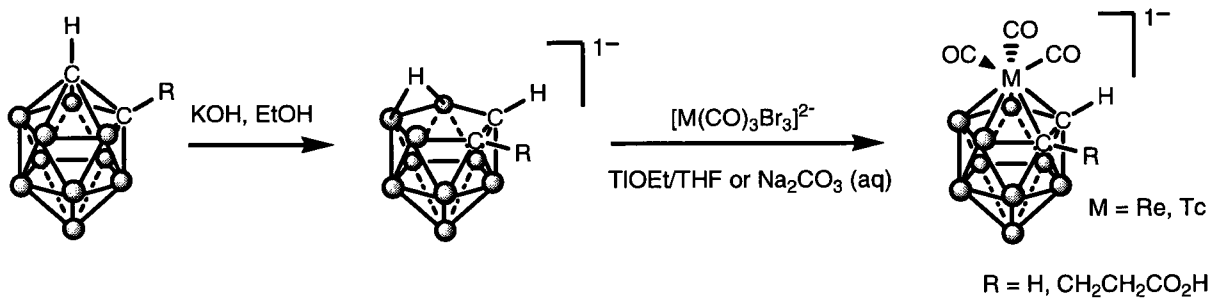

Scheme 2.3: Synthesis of carborane $[M(CO)_3]^+$ complex[58]

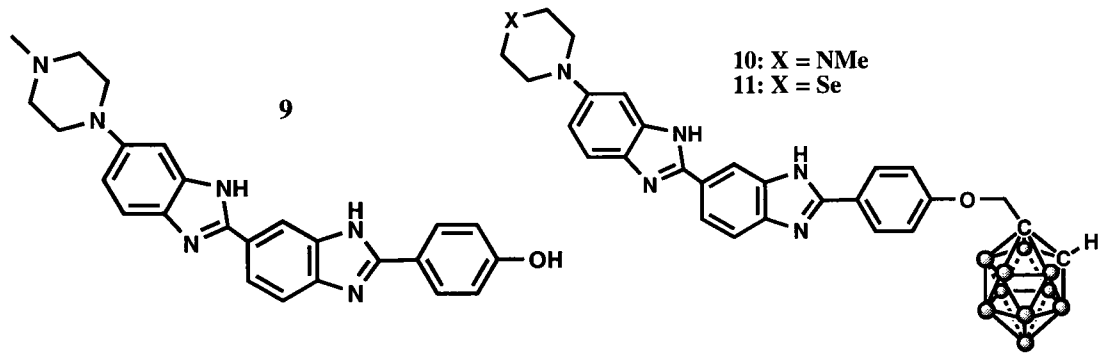

Figure 2.8: Compound (**9**) binds to grooves in DNA. Compounds (**10**) and (**11**) are similarly modeled.[59]

As previously discussed, there are a few techniques which can be applied for imaging with boron isotopes. Unfortunately ^{10}B and ^{11}B isotopes are both quadrupolar, which causes broad signals and sometimes indistinguishable NMR spectra. Magnetic Resonance Imaging (MRI) is a medical imaging technique which utilizes the same theory as NMR, although the instrumentation is arranged horizontally, and with a very wide bore probe. Single Point Imaging (SPI) is a technique where only one data point is acquired to minimize problems with ^{11}B's short relaxation times. SPI has poor signal to

noise ratio, as multiple data points are needed for strong signals for most other NMR active nuclei.[60] There are a few problems with clinical boron MRI applications. First, the clinical instruments would need upgrades and reprogramming for ^{11}B detection. Commonly utilized nuclei are already programmed in current MRI systems, but the upgrades would only apply to existing MRI's as new ones could be programmed during assembly. Another problem would be performing double the scans for each subject. Since ^{11}B isotope is much more abundant than ^{10}B, and has a spin of 3/2, it is much easier to detect with NMR/MRI. However, most pharmaceuticals utilize ^{10}B enriched samples for applications with BNCT; patients would have to be scanned with ^{11}B compounds for the necessary data before being administered with ^{10}B compounds. Boron might be better applied in MRI imaging if it was tagged with a better isotope, like ^{19}F. The inclusion of such an isotope would negate the need to undergo ^{11}B scans, and so patients would only need to be administered ^{10}B enriched compounds.[61]

Looking at some applications of ^{10}B isotopes other than BNCT, Boron Neutron Capture Synovectomy comes to mind. Radiation Synovectomy has already been applied to severe rheumatoid arthritis, but it has problems with isotope leakage and significant staff exposure to radioactive material. Alternative approaches included Boron Neutron Capture Synovectomy (BNCS), where the daughters of the boron neutron capture process destroy the biological function of arthritic tissue. This process minimizes impact to surrounding anatomical structures, like bone and cartilage, since the BNCS compounds would have tethered selective targeting agents.[62] BNCS also has an advantage over traditional Radiation Synovectomy since ^{10}B is stable and not radioactive. After treatment, the risk of radiation leakage is also eliminated. A group lead by Yanch

concluded that BNCS would be appropriate for ablating problematic rheumatoid arthritis as long as selective targeting agents are developed.[62] Both Hawthorne and Valliant groups have pursued this area of research, where the former developed a carborane agent with liposome delivery agents[63], and the latter developed a corticosteroid ester agent which is taken up by inflamed tissues[64]. The liposomes incorporate compound **12** in their bilayer, and species **13** is encapsulated in an aqueous core of the liposomes. The results ensuing from this research were encouraging. The steroid method is being pursued further.

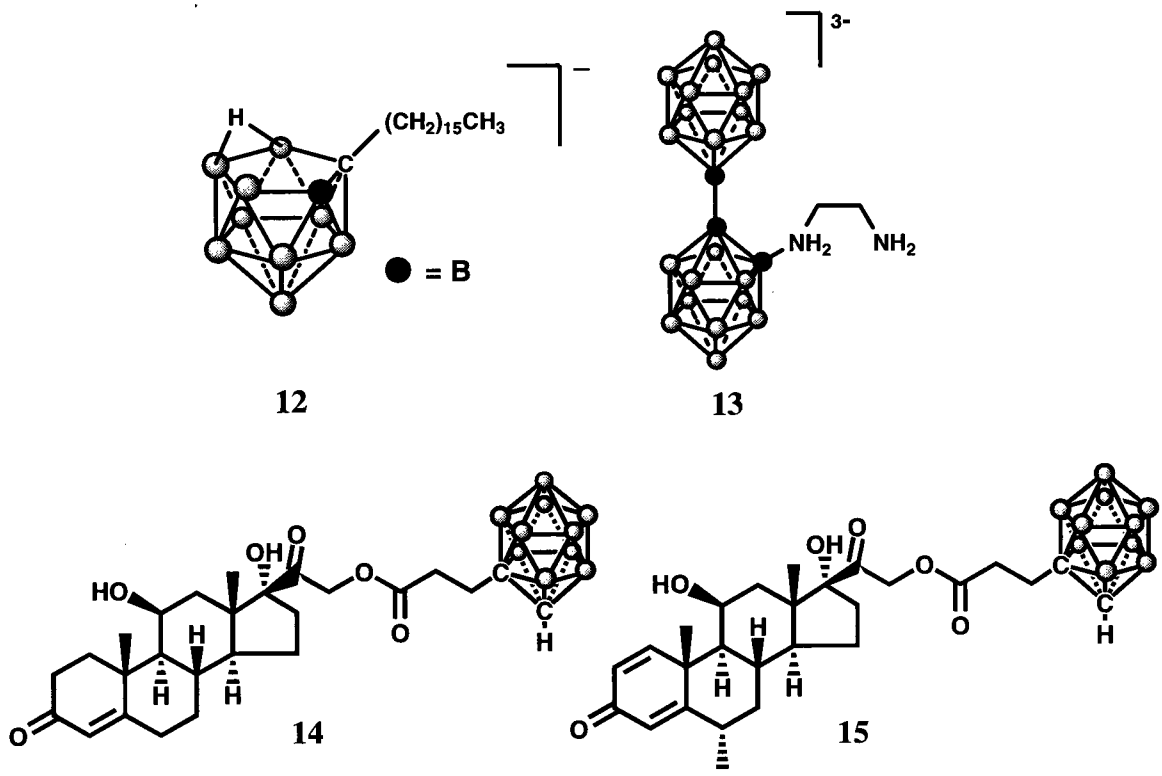

Figure 2.9: Compounds **12** and **13** are taken up by liposomes[63], and Carboranyl ester compounds **14** and **15** based on corticosteroids.[64]

As detailed in the short review above, there are many different ways of incorporating carborane into the medicinal field. Many examples, like intercalators, pharmacores, and radiopharmaceuticals, demonstrated the need for an agent which can both deliver boron and have highly selective targeting functionalities. There are many instances where the process has been researched and the targeting functionality is one key final step to be pursued. All of the above methods, including the highly adaptable BNCT, are perfect examples of the range of applications for carborane clusters. Following is a detailed account on functionalized carboranes in the preliminary steps of this research project, where various reaction paths have been tested and Raman spectra collected for future imaging applications.

2.2 Discussion

The preliminary experiments conducted at the initial stage of the project were to examine the B-H and C-H stretch from the Raman spectra. Most compounds were produced to study the reactivity of the carborane isomers. As a result, many of the compounds which resulted in mixtures were not further purified, nor were they analyzed by Raman spectroscopy. A general reaction pathway for the common organic functionalizations was applied to all of the carborane isomers. This is illustrated in Scheme 2.4. Carborane is deprotonated by butyl lithium under an atmosphere of N_2, and the resulting lithio carbanion salt acts as a nucleophile and attacks an electrophilic center on the organic reagent. The reaction is then quenched by acid to produce the remaining CH on carborane. This is a precautionary step, as only one equivalent of butyl lithium would have been added to the solution, however the butyl lithium reagent is most often found in concentrations exceeding 1.6 molar since hexanes are volatile. Double functionalizations do not require acidic quenching, and the products can be collected directly. As previously mentioned, the different isomers of carborane have acidities that increase with decreasing CH proximities. That is to say, the acidities follow *ortho* > *meta* > *para*, which affect the conditions for various functionalizations. The meta and para isomers require rigorous conditions for deprotonations, which is why these are performed at room temperature. The ortho experiments are conducted at -22°C. On the other hand, if single deprotonation is needed, the reaction must be gentle enough so as to limit double deprotonation. Double deprotonation and disproportionation can be minimized by having a very dilute solution.[44] Unfortunately, this is not always possible when conducting the

reaction in a dry environment, as the solvents are only dispensed from 1 L bottles and the space for the reaction is restricted. These reactions are deprotonated by adding cold butyl lithium drop wise over a few minutes, while stirring, to ensure an even concentration.

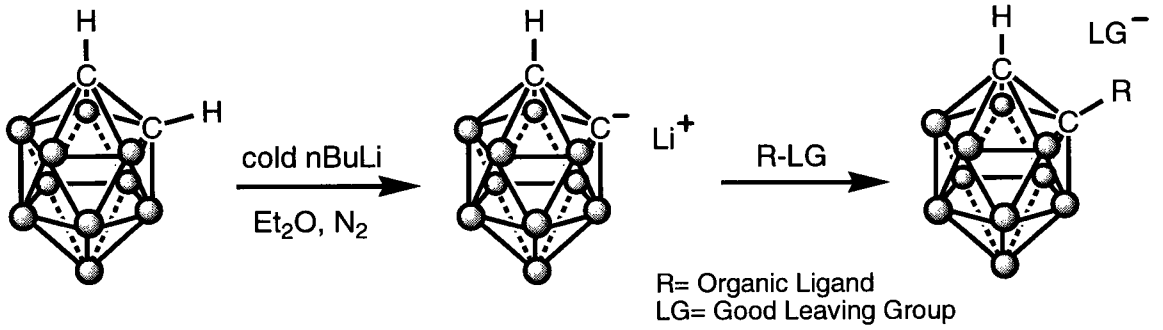

Scheme 2.4: General reaction scheme for functionalizing carborane. Please note any isomer can be utilized, but only the *ortho* is illustrated here.

The functionalized carborane reactions enumerated below only represent a short library of possible functionalizations. Many of these reactions were repeated for higher yields or larger amounts of product, but due to problems with disproportionation it was very difficult to obtain mono substituted products. The products discussed range from *ortho* and *meta* isomers, as well as various organic ligands including ketones, aldehydes, and esters.

The first compound produced was a ^{t}butyl ketone, 1,2-di-^{t}butylacetyl-1,2-dicarba-*closo*-dodecaborane (**16**), since the alkyl groups would produce large CH peaks in the Raman spectra. The *ortho*-carborane isomer was dissolved in diethyl ether under inert atmosphere, and one 1.1 equivalents of cold n-butyl lithium was added dropwise. This produced a salt mixture with white precipitate, and the reaction was slowed by storing in

the freezer at -22°C. The solution was stored here for 25 hours, although one hour at room temperature is sufficient for deprotonation of the *ortho* isomer. When the trimethylacetyl chloride was added, the salt changed composition, from a heavy, grainy salt, to a more powdery precipitate. This is resulting from the new lithium chloride salt contained in the solution. The solution was again placed in the freezer, for 2.5 hours, and then subsequently removed from the inert atmosphere for the work up steps. The lithium chloride had not dissolved completely in the diethyl ether, and so it was removed by suction filtration. The diethyl ether was removed utilizing a Rotovap, and subsequently water was added for extractions. The product was extracted into hexanes, and dried to a white solid with a fairly high yield of 70.1%.

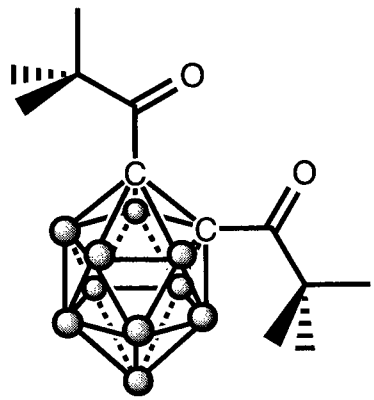

16

Once the proton NMR had been collected, the spectrum illustrated that the disubstituted product was produced, when the actual sought after product was the mono substituted. This can be seen clearly by the missing CH singlet from carborane in the δ 3.5 ppm area, and the large CH singlet in δ 1.3 ppm area which accounts for 18 hydrogens. In this case, the broadened BH peaks integrated for 10 protons, which are not always clear, since there exists considerable broadening from the quadrupolar ^{10}B and ^{11}B isotopes. The formation of the disubstituted product indicates the possibility that the butyl lithium added was concentrated more than 1.6M. This could result from an older bottle of the solution having problems with the Sureseal cap. As a result, the added trimethylacetyl chloride should have been measured for only 1.1 equivalents, as the additional reagent produced the disubstituted product. The resulting Raman spectrum clearly exhibited two

very strong signals, one for the BH stretch and one for the CH stretch, with almost equal intensity. The goal of this compound was to produce very distinct Raman signals, and to examine the intensity of the BH stretch with a CH handle. The OH vibrational stretch is observed at 1713cm^{-1} with a medium intensity.

The next phase of functionalizations involves attaching aldehyde groups to various carborane isomers. The reason was to somehow attach these to the nanoparticle for imaging, however this was never explored as a better ligand was applied, which will be discussed later. Nevertheless, here the functionalizations are presented for synthetic pathways and information. The first compound of this aldehyde library synthesized was an *ortho*-carborane formyl derivative, 1-formyl-1,2-dicarba-*closo*-dodecaborane (**17**). This compound was synthesized in the fume hood, under a stream of N_2. *Ortho*-carborane was dissolved in dry diethyl ether (obtained from glove box) and the solution was stirred. Under the stream of N_2, 1.1 equivalents of cold n-butyl lithium were added dropwise, through a septum *via* syringe. The solution was refrigerated for 2.5 hours, and then removed for the addition of methylformate. The solution was then refrigerated for an additional 2 hours, and then quenched with dilute HCl. This step is to ensure that the remaining CH on carborane remains protonated. The diethyl ether was removed by Rotovap, and the aqueous solution was extracted with hexanes. The resulting 23 mg of product was collected with a yield of 18.9%. Once the NMR spectrum was collected and analyzed, it was determined that the mono product was indeed produced. A peak at δ 9.3 ppm indicates the aldehyde proton, and a peak at 4.08 ppm is present for the remaining CH. As usual, the BH range of the spectrum is extremely broadened by the two boron isotopes, which ranged between δ 3.6 and 1.2 ppm.

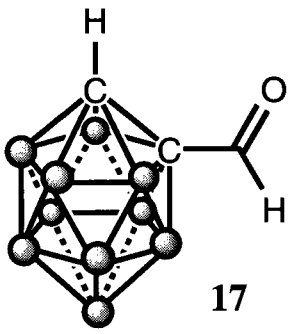

17

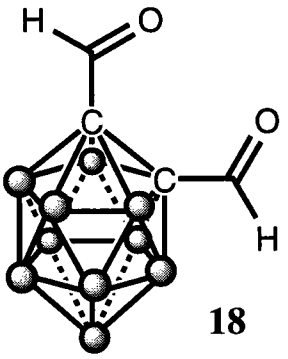

18

The disubstituted product, 1,2-diformyl-1,2-dicarba-*closo*-dodecaborane (**18**), was also attempted. The reaction was conducted the same manner as **17**, only instead of 1.1 equivalents of n-butyl lithium and methylformate, 2.2 equivalents were added. Unfortunately, the spectrum produced was not clear. It is possible that a different product was formed during the synthesis, one which has a cross reaction between the two pendant aldehydes. Various attempts were unsuccessful in producing the desired product (**18**).

The next compound attempted was the *meta*-carborane derivative of the mono-aldehyde, 1-formyl-1,7-dicarba-*closo*-dodecaborane (**19**). This compound was synthesized using similar steps as compound (**17**). *Meta*-carborane was dissolved in dry diethyl ether under an N_2 atmosphere, where it was then deprotonated with 1.1 equivalents of cold n-butyl lithium, added dropwise. It is important to note that the *meta* isomer does not precipitate when deprotonated, until a short range at -10°C. The solution was refrigerated for 2 hours, and the methyl formate was added. The solution was again refrigerated for 2 hours, at which point the solvent was removed by Rotovap. Water was added to the flask, and the product was extracted into hexanes. Once the hexanes were removed *in vacuo*, 8 mg of the solid product was collected. This synthesis resulted in a

very poor yield of 6.7%; it is possible that since the HCl quenching step was omitted, most of the product remained deprotonated, thus never extracting into the hexane layers. Fortunately, enough product was obtained to collect an NMR spectrum.

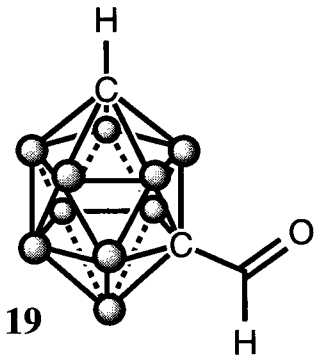

19

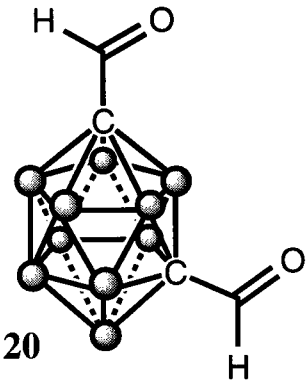

20

The proton NMR with ^{11}B decoupling was acquired and analyzed for product formation. A peak present at 9.07 ppm was indicative of the formyl proton. However, a significant shoulder having a shift of 9.05 ppm could indicate either a mixture with a disubstituted compound, or some other impurities were present. A shift present at 3.18 ppm was indicative of the remaining CH proton, however, this too had a shoulder associated with it. The remaining peaks between 2.59 ppm and 2.15 ppm are associated with the BH bonds. No further purifications or analyses were conducted because of the low yield.

The synthesis of the disubstituted *meta* product, 1-7-diformyl-1,7-dicarba-*closo*-dodecaborane (**20**), was expected to work since the carbon atoms are not as close in proximity as with the *ortho* isomer. *Meta*-carborane was dissolved in dry diethyl ether, under an inert atmosphere, and deprotonated with 2.2 equivalents of cold n butyl lithium. The solution was stored in the refrigerator for 2 hours, and methyl formate was added.

The solution was replaced in the refrigerator for 2 hours to allow the reaction to proceed. The diethyl ether was then removed by Rotovap, and water was added to the flask. The products were extracted into hexanes, where the final compound **20** was recovered once the solvents were removed. The resulting yield is low, 38.1%, however enough product was collected for various analyses.

The proton NMR spectrum with ^{11}B decoupling was recorded and analyzed for product formation. It was concluded that a mixture of compounds had been produced. This is evident from the appearance of two peaks in the δ 9 ppm range, one of which integrates for half of the other peak. Also, there are a few peaks which do not belong to the BH range, δ 3.16 and δ 2.85 ppm. The δ 2.85 ppm CH peak characteristic of *meta*-carborane starting material, and integrates for a larger amount than the δ 3.16 ppm peak. The integrations are not quantitative, nor do they correlate to each other directly, since the ^{10}B quadrupolar isotope is still coupling and has a broadening effect. It has been concluded that three compounds are present in this mixture: the disubstituted product, which has a single CH peak at δ 9.05 ppm; the monosubstituted product, where the peak at δ 9.07 ppm integrates for half of the δ 9.05 peak, and the CH peak is present at δ 3.16 ppm; and the starting material, where a CH peak accounting for two protons is present at δ 2.85 ppm. No further experiments were conducted to separate these compounds.

The last two compounds in this short library are the ester derivatives. First, the mono-substituted *ortho*-carborane ester compound, 1-ethyl ethanoate-1,2-dicarba-*closo*-dodecaborane (**21**), was attempted. *Ortho*-carborane was dissolved in dry diethyl ether under an inert atmosphere, where 1.1 equivalents of cold n-butyl lithium were added. The lithium salt formed and precipitated, and the solution was placed in the freezer for 2.5

hours. Diethyl carbonate was then added, and the solution was stirred and replaced in the freezer for another 2 hours. Once the solution was removed from the N_2 atmosphere it was quenched with dilute HCl, which formed a white precipitate. The organic solvent was removed *via* Rotovap, and the remaining product was extracted into hexanes. The resulting white product had a yield of 34.5%, similar to **20**.

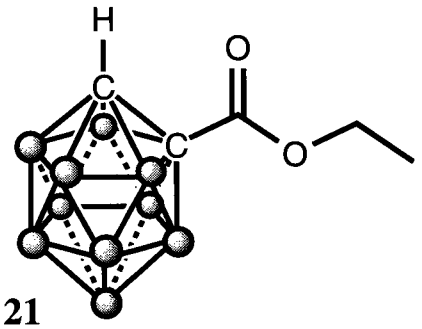

21

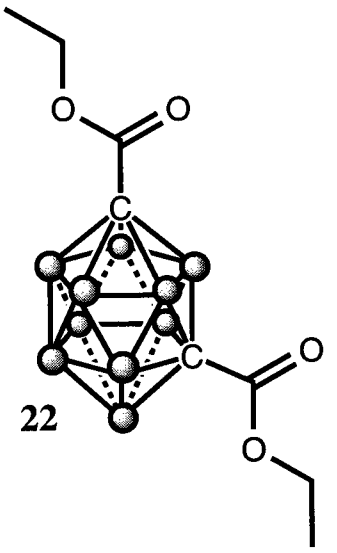

22

The proton NMR with ^{11}B decoupling spectrum was acquired and analyzed for product formation. This particular spectrum was very clear to decipher, as the CH_2 and CH_3 groups are present with coupling signals. A quartet at δ 4.25 ppm is indicative of the CH_2 group, while a singlet at δ 4.05 ppm is present for the CH. The remaining triplet signal for the CH_3 group is present at δ 1.30 ppm. As usual, the BH signals are present at δ 2.35, δ 2.21, and δ 2.16 ppm. It is interesting to note that the singlet at δ 4.05 ppm for the CH on carborane is shifted downfield; this can be attributed to an increase in aromaticity and electron withdrawal by the adjacent ester group contained on the other carbon.

A crystal was also obtained for this compound, seen in Figure 2.10. The bond lengths within *o*-carborane vary from 1.611 Å (C6-C7) to 1.797 Å (B11-B15). Surprisingly, the bonds running from the lower 5 borons to B14 are not the longest, they are only ~1.781 Å. The shortest bond as expected is 1.188 Å, between C8 and O3. The angle between 3 of the bottom 5 atoms (B15-B11-B13) is comparable to the angle on the capping boron (B11-B14-B17), which are both at ~107.5°. The angles of the bonds which zigzag in the midsection of carborane vary between ~60-64°. When examining the angles surrounding C8, it is revealed that the Sp^2 120° angles are skewed. C7-C8-O4 is the smallest angle, at 110.2°. Even with all surrounding angles added together, they only result in 348.4°. It is observed that upon rotating the crystal model the ethyl acetate ligand is not planar. This may be due to the crystal packing, where perhaps a carborane is stacking on top of C8, which would influence the sterics on the ligand.

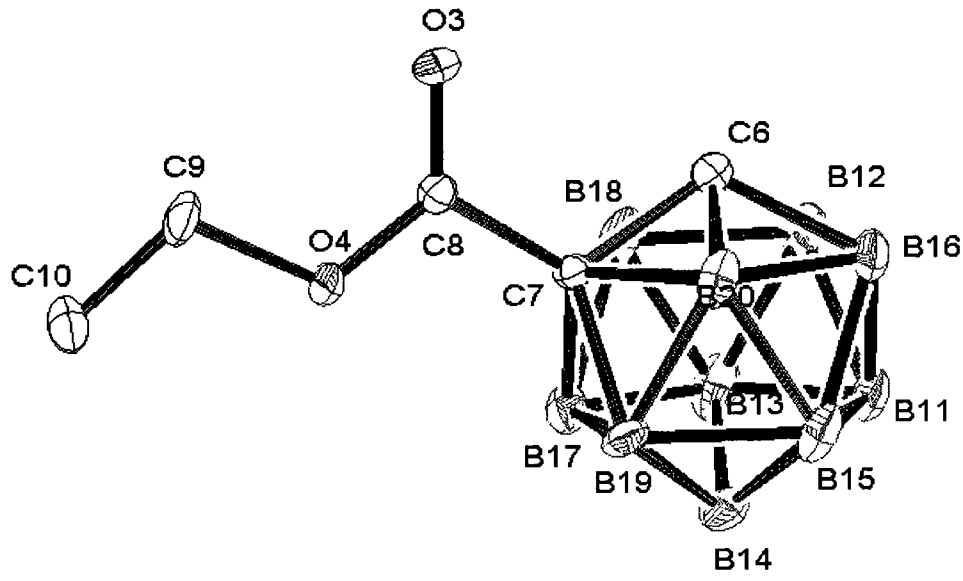

Figure 2.10: Thermal ellipsoid plot showing the molecular structure and atom numbering scheme for **21**. Thermal ellipsoids are drawn at 20% probability.

Table 2.1: Select Bond Distances and Angles for **21**

Atoms	Bond Distances (Å)	Atoms	Bond Angles (°)
C6-C7	1.611(6)	C7-C6-B16	113.2(4)
C6-B20	1.690(8)	B15-B11-B13	107.6(4)
B20-B15	1.767(8)	B16-C6-B12	63.4(4)
B11-B15	1.797(9)	B11-B14-B17	107.7(5)
B19-B14	1.781(8)	B19-B20-B15	60.4(3)
C7-C8	1.529(6)	C6-C7-C8	115.8(4)
C8-O3	1.188(5)	C7-C8-O4	110.2(4)
C9-C10	1.480(7)	C7-C8-O3	122.4(4)

The *meta*-carborane disubstituted ester (**22**) was synthesized following the same general steps as above. *Meta*-carborane was dissolved in dry diethyl ether under an inert atmosphere, and then 2.2 equivalents of cold n-butyl lithium were added slowly. The solution was stirred and placed in the freezer for 2 hours. An excess of diethyl carbonate was added, and the solution was again placed in the freezer for 2 hours. The solution was removed from the inert atmosphere, and quenched with dilute HCl. The organic solvent was removed *in vacuo* and the products were extracted into hexanes. The hexanes were then removed *via* Rotovap, resulting in 147 mg of white precipitate; a yield of 50.7%.

The proton NMR spectrum with ^{11}B decoupled was acquired, and it shows the formation of the disubstituted product. A quartet representing the two CH_2 groups appears at δ 4.18 ppm. The related triplet at δ 1.27 integrates for 6 hydrogens contained on the two CH_3 groups. In between, the BH signals are very different from the starting material; there are many more environments now with the disubstitution. The BH signals appear at δ 2.89, δ 2.61, δ 2.56, δ 2.42, and δ 2.17 ppm. These are quite broadened in contrast to compound **21**, which may be because of the added symmetry of **22**. The

Raman spectrum of **21** shows a strong peak at 2630 cm^{-1}, representing the BH vibrations. A broader medium peak at 2944 cm^{-1} is observed for the CH vibrations of the molecule. A weak peak for the C=O vibration is observed at 1752 cm^{-1}.

2.3 Experimental

General

Reagents and solvents used were obtained form Aldrich Chemicals, with the exception of the carborane isomers, which were purchased from Katchem Ltd. NMR spectra were recorded on a Bruker Avance 300 MHz, or 500 MHz NMR spectrometer using the residual protons of the deuterated solvent for reference. Raman spectroscopy was acquired with a microRaman system (LabRAM HR, Horiba Jobin Yvon). The Raman spectra were acquired by 632.8 nm irradiation at a power density of ~ 10^5 W/cm^2. X-ray crystallography experimental for **21** is contained in Appendix A. Mass Spectroscopy Electron Ionization was acquired with a Kratos Concept Tandem Mass Spectrometer by the University of Ottawa Mass Spectroscopy Center.

1,2-di-^{t}butylacetyl-1,2-dicarba-*closo*-dodecaborane (**16**)

To a solution of *o*-carborane (0.100 g, 0.694 mmol) in dry diethyl ether was added cold 1.6 M nBuLi (0.50 ml, 0.77 mmol) slowly, under N_2 atmosphere. The solution was stirred until white salt was homogenous, and placed in the freezer for 25 hours. Trimethylacetyl chloride (0.30 ml, 2.4 mmol) was added, and the white salt changed from crystalline to powder in appearance. The solution was placed in the freezer for 2.5 hours at -22°C, and subsequently removed from the glove box. Precipitate was removed by vacuum filtration. The diethyl ether was removed *in vacuo* from the filtrate. A white powder was collected (0.152g, 0.487 mmol) with an isolated yield of 70.1%. ^{1}H NMR (300 MHz, $CDCl_3$) δ

3.61-1.45 (m, 10H, BH), δ 1.33 (s, 18H, CH_3); $^{13}C\{^1H\}$ (500MHz, $CDCl_3$) δ 195.63 ppm (C=O), δ 84.45 ppm (C-BH), δ 47.99 ppm (C-Me_3), δ 27.69 ppm (CH_3); Raman Spectra: 1713 cm^{-1} (medium, C=O), 2628 cm^{-1} (strong, BH), 2932 cm^{-1} (strong, CH).

1-formyl-1,2-dicarba-*closo*-dodecaborane (**17**)

A solution of *o*-carborane (0.102g, 0.707 mmol) in 6 ml diethyl ether was stirred at room temperature, under a stream of N_2. Cold 1.6 M nBuLi (0.48 ml, 0.77 mmol) was added drop wise through a syringe over 2 minutes, and the solution was stirred and placed in refrigerator for 2.5 hours. Methyl formate (0.30 ml, 4.85 mmol) was subsequently added, and the solution was refrigerated for 2 hours. The solution was removed, and 2ml dilute HCl (~4M) was added. Diethyl ether was removed *in vacuo* and the resulting aqueous mixture was extracted with hexanes (4 x 20 ml). Organic layers were combined, and dried with $MgSO_4$. The organic extracts were then dried *in vacuo* and a solid was collected (0.023g, 18.9 % yield). ^1H NMR (300 MHz, $CDCl_3$) δ 9.303 (s, 1H, OCH), δ 4.08 (s, 1H, CH), δ 3.62-1.20 (m, 10H, BH).

1,2-diformyl-1,2-dicarba-*closo*-dodecaborane (**18**)

A solution of *o*-carborane (0.100g, 0.694 mmol) in 6 ml diethyl ether was stirred at room temperature, under a stream of N_2. Cold 1.6 M nBuLi (0.96 ml, 1.54 mmol) was added drop wise through a syringe over 2 minutes, and the solution was stirred and placed in refrigerator for 2.5 hours. Methyl formate (0.2 ml, 3.0 mmol) was subsequently added,

and the solution was refrigerated for 2 hours. The solution was removed, and 2ml dilute HCl (~4M) was added. Diethyl ether was removed *in vacuo* and the resulting aqueous mixture was extracted with hexanes (4 x 20 ml). Organic layers were combined, and dried with $MgSO_4$. The organic extracts were then dried *in vacuo* and a solid was collected (0.115g, 82.8 % yield). ^1H {^{11}B} NMR (500 MHz, $CDCl_3$) δ 9.26 ppm (s), δ 9.24 ppm (s), δ 8.08 ppm(s), δ 5.59 ppm (d), δ 5.28 ppm (s), δ 5.15 ppm (s), δ 2.24 (m, BH).

1-formyl-1,7-dicarba-*closo*-dodecaborane (**19**)

A solution of *m*-carborane (0.100g, 0.694 mmol) in 15 ml diethyl ether was stirred at room temperature, under a stream of N_2. Cold 1.6 M nBuLi (0.48 ml, 0.77 mmol) was added drop wise through a syringe over 2 minutes, and the solution was stirred and placed in refrigerator for 2 hours. Methyl formate (0.15 ml, 2.4 mmol) was subsequently added, and the solution was stirred and replaced into the refrigerator for 2 hours. Diethyl ether was then removed *in vacuo* and 15 ml H_2O was added to the round bottom. The solution was extracted with hexanes (4x 20 ml), and the organic layers were collected and dried with $MgSO_4$. Solvent was removed *in vacuo* and a solid was collected. (8 mg, 6.7% yield). ^1H {^{11}B} NMR (500 MHz, $CDCl_3$) δ 9.07 ppm (s, 1H, OCH), δ 3.18 ppm (s, 1H, CH), δ 2.59 ppm (s, BH), δ 2.44 ppm (s, BH), δ 2.34 ppm (s, BH), δ 2.29 ppm (s, BH), δ 2.15 ppm (s, BH).

1-7-diformyl-1,7-dicarba-*closo*-dodecaborane (**20**)

A solution of *m*-carborane (0.100g, 0.694 mmol) in 15 ml diethyl ether was stirred at room temperature, under a stream of N_2. Cold 1.6 M nBuLi (0.97 ml, 1.56 mmol) was added drop wise through a syringe over 2 minutes, and the solution was stirred and placed in refrigerator for 2 hours. Methyl formate (0.44 ml, 7.09 mmol) was subsequently added, and the solution was stirred and replaced into the refrigerator for 2 hours. Diethyl ether was then removed *in vacuo* and 15 ml H_2O was added to the round bottom. The solution was extracted with hexanes (4x 20 ml), and the organic layers were collected and dried with $MgSO_4$. Solvent was removed *in vacuo* and a solid was collected. (53 mg, 38.1% yield). ^1H $\{^{11}B\}$ NMR (500 MHz, $CDCl_3$) δ 9.07 (s, 1H, HCO), δ 9.05 (s, 2H, HCO), δ 3.16 (s, 1H, CH), δ 2.85 (s, 2H, CH), δ 2.59 (s, BH), δ 2.41 (d, BH), δ 2.34 (t, BH), δ 2.23 (s, BH).

1-ethyl ethanoate-1,2-dicarba-*closo*-dodecaborane (**21**)

To a solution of *o*-carborane (0.100 g, 0.694 mmol) in dry diethyl ether was added cold 1.6 M nBuLi (0.48 ml, 0.77 mmol) slowly, under N_2 atmosphere. The solution precipitated, and was stirred and refrigerated for 2.5 hours. Diethyl carbonate (0.29 ml, 2.4 mmol) was added; the solution was again stirred and placed in refrigerator for 2 hours. The solution was removed from N_2 atmosphere, and was quenched with 2ml of dilute HCl (~ 4M). Diethyl ether was removed *in vacuo*, and 10 ml H_2O was added. The aqueous mixture was extracted with hexanes (4x 20 ml). The combined organic extracts

were dried with $MgSO_4$, and the solvent was removed *in vacuo*. A white crystalline solid was collected (52 mg, 34.5% yield). ^1H $\{^{11}B\}$ NMR (500 MHz, $CDCl_3$) δ 4.25 (quartet, 2H, CH_2), δ 4.05 (s, 1H, CH), δ 2.35 (d, BH), δ 2.21 (s, BH), δ 2.16 (s, BH), δ 1.30 (t, 3H, CH_3); $^{13}C\{^1H\}$ (500 MHz, $CDCl_3$) δ 161.02 ppm (C=O), δ 68.98 ppm (C-BH), δ 64.89 ppm (CH-BH), δ 56.89 ppm (CH_2), δ 13.75 ppm (CH_3); X-ray Crystallography solved, see page X. Raman Shift: 1752 cm^{-1} (weak, C=O), 2630 cm^{-1} (strong, BH), 2945 cm^{-1} (medium, CH).

1,7-diethyl ethanoate-1,7-dicarba-*closo*-dodecaborane (**22**)

To a solution of *m*-carborane (0.145 g, 1.005 mmol) in dry diethyl ether was added cold 1.6 M nBuLi (0.70 ml, 1.12 mmol) slowly, under N_2 atmosphere. The solution was stirred and refrigerated for 2 hours. The salt precipitated only at -10°C. Diethyl carbonate (0.41 ml, 3.40 mmol) was added; the solution was again stirred and placed in refrigerator for 2 hours. The solution was removed from the N_2 atmosphere, and quenched with 10% HCl. Diethyl ether was removed *in vacuo*. The remaining aqueous solution was extracted with hexanes (4x 20 ml) and organic extracts were dried with $MgSO_4$. Solvent was removed *in vacuo* and 0.147g of product was recovered (50.7% yield). ^1H $\{^{11}B\}$ NMR (500 MHz, $CDCl_3$) δ 4.18 (quartet, 4H, CH_2), δ 3.16 (s, BH), δ 2.89 (s, BH), δ 2.61 (s, BH), δ 2.56 (s, BH), δ 2.42 (s, BH), δ 2.17 (s, BH), δ 1.27 (t, 6H, CH_3).

Chapter 3

Imaging Cells through Anti-EGFR Targeting Antibodies

3.1 Introduction

As previously discussed, the use of SERS for biological imaging has eclipsed the use of fluorescence because of its impressive enhancement and tuning variability. However, something not mentioned is how exactly the nanoparticles, adsorbed analytes, and cells all come into play together. Most literature research on the enhancement of Raman scattering with nanoparticles has focused only on one type of adsorbed compound. This is the molecule which bonds to the surface of the nanoparticle through its valence electrons, for which the SERS enhancement will reveal spectroscopic information. There are other methods of functionalizing the nanostructures to get information on not only the adsorbant, but cellular information and functions as well. There are two fundamental compositions for SERS in biosensing: intrinsic and extrinsic detection. In intrinsic detection, the analyte is adsorbed onto the nanostructure, where the Raman spectrum is obtained directly (same process as described previously). This process is used to identify the analyte, and in this case SERS would be used to augment the Raman spectrum. Figure 3.1 a. represents molecules adsorbed onto the nanostructure surface. For Figure 3.1 b. a similar method is applied, called indirect intrinsic detection, where the spectra are collected before and after to identify specimens (ex. antibodies) captured onto the nanostructure surface. Extrinsic detection is depicted in Figure 3.1 c., a Raman reporter is tethered onto the nanoparticle surface, where it provides an imaging signal for detection. Another targeting specimen is attached to the nanostructure, either

directly on the surface alongside the Raman reporter, or outside on the surface of a SiO_2, TiO_2 or polymer shell. This allows for selective targeting since the targeting specimen and the Raman reporter can be varied separately on the nanostructure.[65]

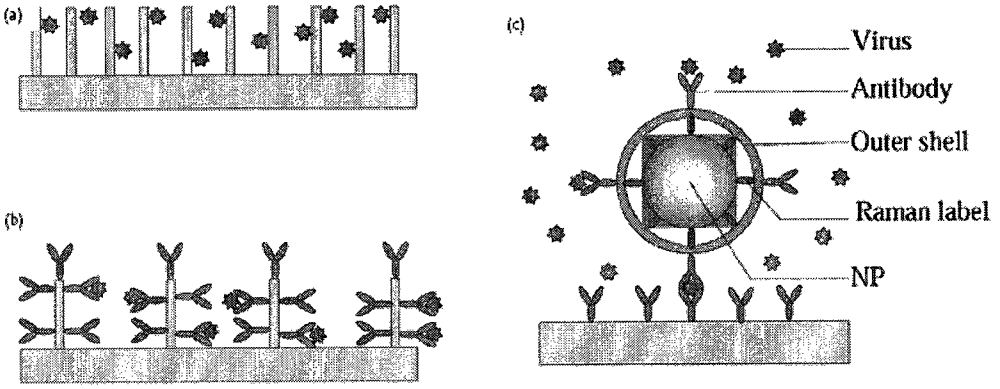

Figure 3.1: Different SERS detection arrangements. a) Direct Intrinsic Detection, b) Indirect Intrinsic Detection, c) Extrinsic Detection.[65]

In our research we apply the extrinsic detection method, where we can tune the Raman reporter and targeting antibody separately. Since carboranes have significant concentrations of B-H bonds in their clusters, thiol carborane has been applied to the synthesis of the functionalized nanoparticle. Other reagents in the synthesis include polyethylene glycol-SH groups for increased solubility, and anti-Epidermal Growth Factor Receptor (EGFR) antibodies. EGFR is a cell surface receptor, and its overexpression is associated with many different types of cancers, since mutations lead to overactivity and uncontrollable cellular division.[66] By utilizing anti-EGFR antibodies, it is possible to target carcinomas. EGFR is overexpressed in many cancers on the order of $\sim 10^5$ receptors per cell.[67] These receptors are present as dimers and cluster in groups of

~10-50.[68] A new pharmaceutical called Tarceva targets EGFR to treat lung cancer and pancreatic cancer. The testing group showed a 60% response rate, which is superior to response rates for chemotherapy.[69]

The first *in vivo* application of plasmon coupling for cellular imaging of cancerous cells was published in 2007. Previously, many studies had been conducted utilizing imaging techniques on *in vitro* assays. The *in vivo* assay applied dark field imaging techniques with gold nanoparticles; the cellular receptor used was Epidermal Growth Factor Receptor. Since quantum dots are highly toxic, and both quantum dots and fluorescent dyes undergo photobleaching[70], gold nanoparticles were chosen as the imaging platform. EGFR was chosen as the target, since it is associated with carcinogenesis of some epithelial cancers which include lung, cervical, and oral cavity cancers.[71] EGFR levels significantly increase as the cancer progresses from dysplasia to invasion, and naturally dimerize and aggregate on the cell surface.[72] The research was performed on human cervical biopsy tissue, as well hamster cheek pouches and phantom assays. Resulting spectral changes were visible, where unlabeled cells had a green glow, and labelled cells were very bright orange through dark field imaging (Figure 3.2). Even though both samples had the same concentration of gold nanoparticles, the scattered intensities of cancerous cells correlated with increased EGFR concentration. Similar research performed utilizing fluorescent dye labelling was not nearly as indicative for site specific binding. The fluorescent dye signal had a linear relationship with the number of fluorophores applied, in contrast to the nanoparticles, and it also has a background signal due to unbound dye. It was concluded that approximately 40% more contrast agents were delivered to abnormal tissue versus normal tissue. The next conclusion is staggering: an

increase of 11 fold intensity of reflectance signal which was only present for the abnormal tissue, even though both were treated with the same amounts of nanoparticles! This is indicative that the binding to EGFR is pivotal for the imaging of abnormal tissues.[73]

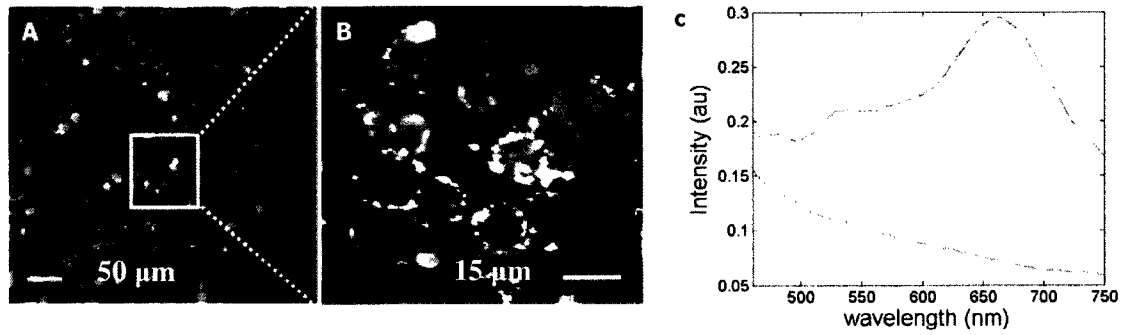

Figure 3.2: Tissue cultures. a) Fluorescent confocal images of transverse section, where EGFR- cells are in green, and EGFR+ cells are in red. b) Overlay of magnetization of (a) with reflectance image. c) Scattering from individual gold conjugates pixels have a maximum of ~530 nm. EGFR mediated aggregation of nanoparticles increase scattering maximum into red region of ~ 650 nm.[70]

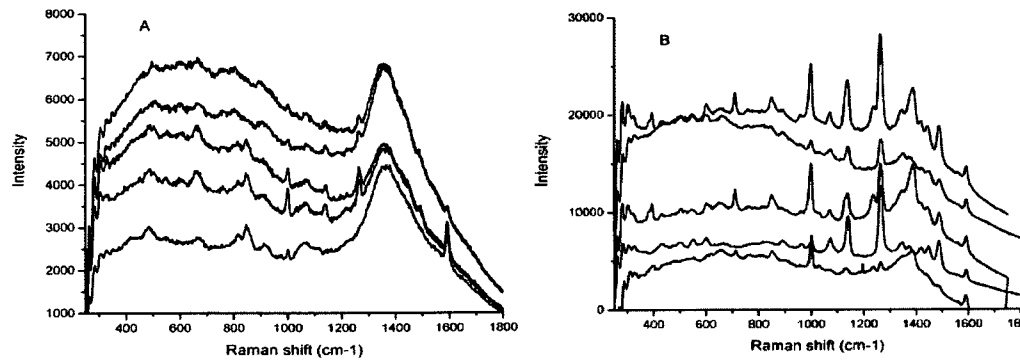

Figure 3.3: (A) SERS of anti-EGFR antibody conjugated gold nanorods normal cells and (B) HSC cancer cells. Raman spectra from five cells for each cell line are shown.

Spectra (B) from the cancer cell samples are stronger (intensity 30000 vs. 7000), sharper, and better resolved than the normal cells. The nanoparticles tethered to the cell through anti-EGFR are easily distinguishable through surface enhanced Raman spectroscopy.[74]

The anti-EGFR antibodies used in our reported research are assembled using the extrinsic detection method as outlined in Figure 3.5. Dithiosuccinimidyl propionate (DTSP) is reacted with the nanoparticle surface and is cleaved to form TSP. TSP has an electrophilic site where the antibody will attack the activated ester group, forming the desired tethered product, see Figure 3.4.[75] There are a few methods to bind the antibody to the antigen once on the cell surface. These can be categorised as primary antibodies and secondary antibodies. Primary antibodies recognise target antigens, whereas secondary antibodies target primary antibodies or antibody fragments. Secondary antibodies are usually labelled probes for detection and cell sorting processes.[76] This method is also used in research if one antibody is much more cost effective versus the other. Figure 3.5 outlines the nanoparticle components and the secondary antibody process.

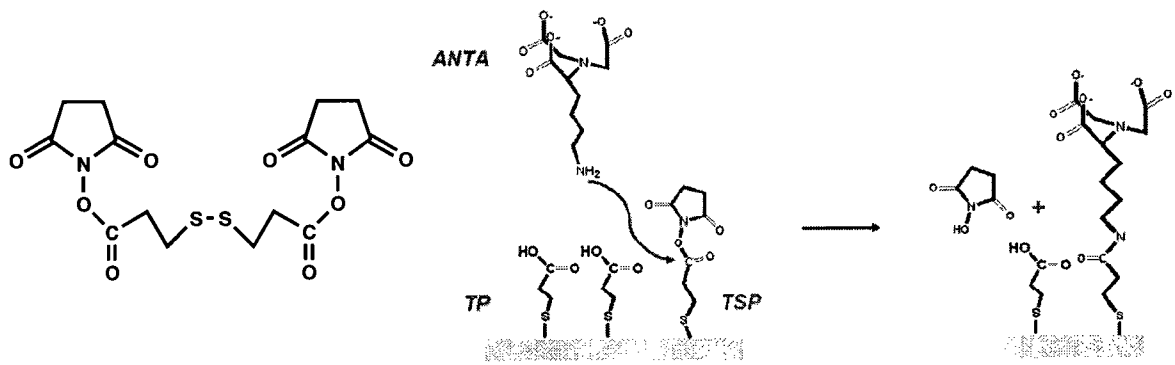

Figure 3.4: Left, Dithiosuccinimidyl propionate (DTSP). Right, nucleophilic attack by amine tethers the antibody (Anta here is a general antibody).[75]

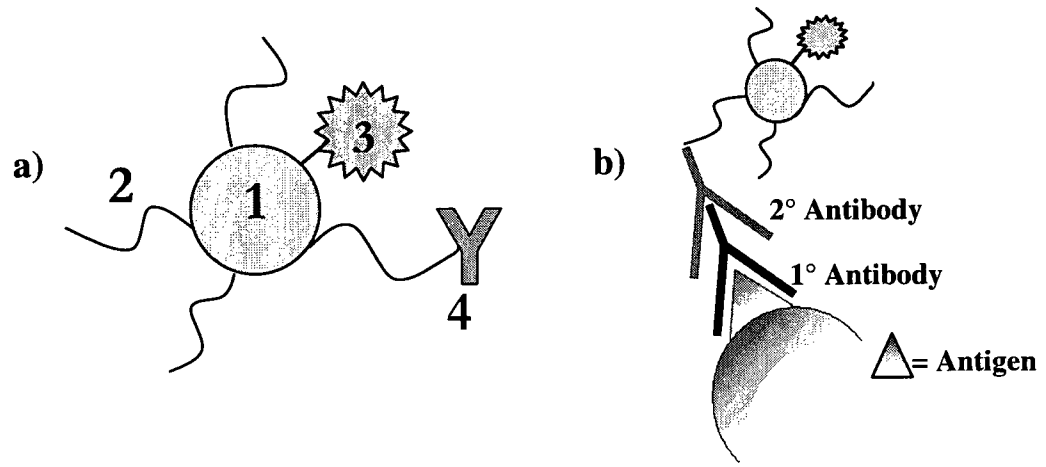

Figure 3.5: a) Assembled components on a silver nanoparticle, where 1) Ag NP, 2) EG_3SH, 3) Carborane thiol, and 4) Antibody. b) Secondary antibodies, tethered by TSP to NP, attaches to Primary antibody anti-EGFR.

Along with SERS, another imaging technique can be applied to the selectively tethered silver nanoparticles, called two-photon luminescence. Two-photon luminescence is a form of multi-photon microscopy, where the process involves absorption of photons and emission from the radiative recombination of electrons from the sp band and the holes in the d band. Gold and silver nanostructures efficiently induce single and two-photon luminescence due to surface plasmon resonance[77]. The functionalized nanoparticles could target specific cells, and two-photon luminescence would be able to image these specific cells. The process can be further utilized by applying the idea of thermal tumour therapy introduced in Chapter 1, where the intensity of the applied laser could be increased to create localized hot sites and destroys the targeted cells. In Chapter 1, the research discussed applied gold nanoshells for this process, but silver nanoparticles have a very similar NIR signature.

In this chapter I will present efforts to employ thiol carborane in an extrinsic labelling and detection method. Specifically, thiol carborane was bonded to Ag nanoparticles which were functionalized with antibody through an amide linkage with thiosuccinimidyl propionate. The carborane functionalized silver nanoparticle is programmed to pinpoint cancer cells utilizing anti-EGFR antibodies. The nanoparticle is also unique because of its two possible therapeutic applications aimed at the malignant tissue. The dose of boron delivered to the cell is very concentrated, and could be used for Boron Neutron Capture Therapy. The second therapeutic application is from two photon luminescence, where the localized heat sources from increasing the laser intensity can destroy the targeted cells. The identification of EGFR targeted cells versus normal cells has been studied utilizing SERS, two-photon luminescence, and scanning electron microscopy.

3.2 Discussion

The experiments and imaging in this chapter were conducted to examine the population of EGFR expressing cancer cells from the population of normal cells utilizing tools such as SERS microscopy, two-photon luminescence, and SEM. The experiments applied 1-mercapto-1,12-dicarba-*closo*-dodecaborane as the Raman reporter tethered onto 25 nanometre silver nanoparticles, with the nanoparticles' increasing the reflected signal enormously. The compiled images from all three aforementioned techniques provided easily discernible information about the targeted regions.

The mercapto-carborane utilized in these experiments for imaging and potential therapeutic purposes, 1-mercapto-1,2-dicarba-*closo*-dodecaborane (**23**) was synthesized in a one step process[78], and is a relatively inert compound, both air and water stable. The carborane is applied in this process because of its high concentration of BH bonds, which have a stretch between 2550-2650 cm^{-1} in the Raman spectrum. Once the mercapto-carborane is tethered to the silver nanoparticle, the Raman transitions are drastically enhanced due to the SERS effect. In Figure 3.6, the Raman signals for free compound **23**, compound **23** bound to the silver nanoparticle, and the resulting hot spot from a cellular surface labelled with B) (the functionalized nanoparticle) are clearly visible in the spectra. While some cellular activity is visible in the range of 1200-1700 cm^{-1}, the BH signals are still significantly greater in intensity. Signals due to the other species contained on the nanoparticle, the EG_3SH and the antibody, are dwarfed in comparison to the well resolved BH absorptions. Other mercapto-carborane reactions

with metal surfaces have been reported, but most of these involve gold films and are not involved in biomedical imaging.

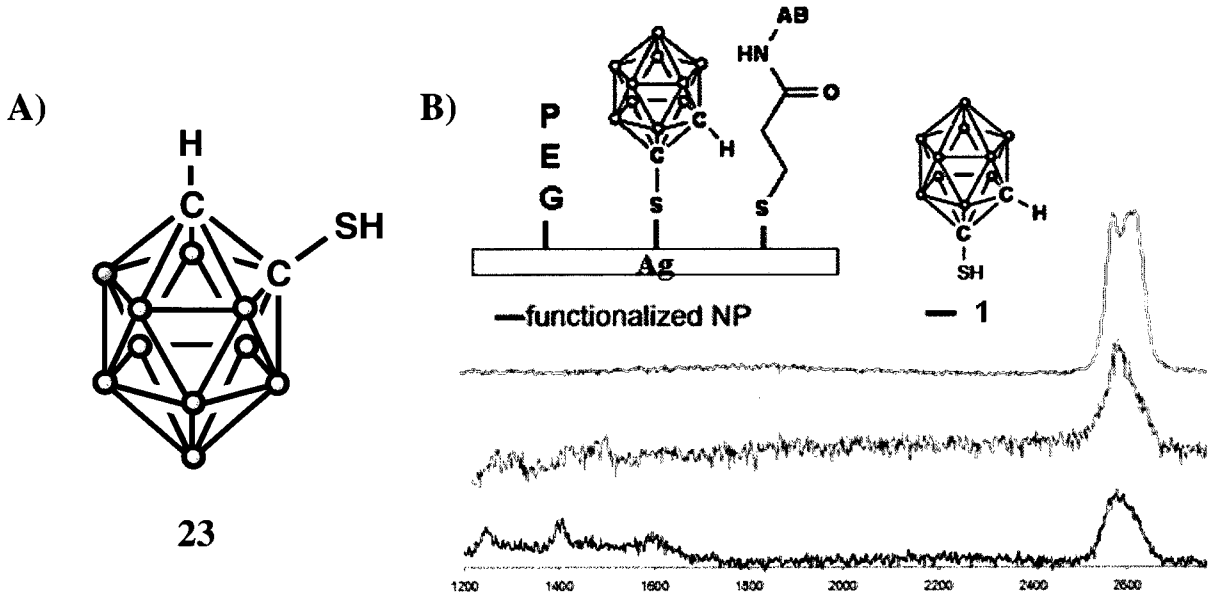

Figure 3.6: A) 1-mercapto-1,2-dicarba-*closo*-dodecaborane (**23**), B) Raman spectra of 1-mercapto-1,2-dicarba-*closo*-dodecaborane (**23**) in red, **23** functionalized to Ag nanoparticle in green, and a hotspot resulting from a cell surface targeted by the functionalized nanoparticle in blue.

The nanoparticle functionalization was experimentally optimized for solubility and stability of the group of components. The 25 nm nanoparticles were coated with 45% 1-mercapto-1,2-dicarba-*closo*-dodecaborane (**23**), 45% 1-mercapto-triethylene glycol (EG_3SH), and 10% thiosuccinimidyl propionate (TSP), as depicted in Figure 3.7. The TSP is required to bind the antibodies to the nanoparticle through the activated ester groups. The polyethylene glycol in use, EG_3SH, provides the nanoparticle with inert

water soluble properties, which allows for cellular studies. The EG_3SH groups also distribute the mercapto-carborane over the nanoparticle surface in order to minimize possible interactions. If the EG_3SH groups are omitted from the nanoparticle functionalization, the nanoparticles aggregate and precipitate in water. If the EG_3SH concentration is increased so its ratio is greater than the mercapto-carborane, then the Raman spectrum resulted in surprisingly absent BH signals. The functionalized nanoparticle must be bound to a secondary antibody in order to detect anti-EGFR on the cell surface.

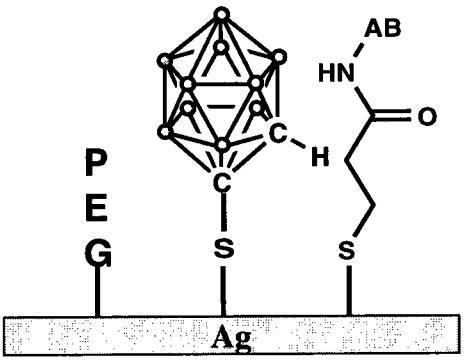

Figure 3.7: Illustration of a functionalized silver nanoparticle surface. From left, 45% EG_3SH polyethylene glycol, 45% mercapto-carborane, and 10% TSP for antibody (AB) conjugation.

The cells employed in this experiment were fixed Huh 7 cells, which were treated with anti-EGFR (rabbit polyclonal IgG) antibodies to detect the EGFR antigens. Once treated with anti-EGFR antibody, the cells were treated with 1 ml of the functionalized nanoparticle solution. Here is where the secondary antibody method is employed, where

the antibody (goat anti-rabbit IgG) anchored to the nanoparticle detects and anchors onto the anti-EGFR antibody already present. The cells were stored for 24 hours, and then the excess nanoparticle solution was washed off, so only tethered nanoparticles remain on the cell surface.

The SERS images were collected for the treated cells, and overlaying high resolution SEM with SERS maps resulted in clear images with additional information. The presence of the receptors on the cell can now be distinguished and pinpointed by observing intercellular structures. Also, the concentration of receptors on the cell surface can be seen and counted, as well as the spatial arrangements. In Figure 3.8a), the bright field optical image of the functionalized-nanoparticle treated cell is shown, as well as the SEM image where the texture of cellular surface is evident (3.9b). In 3.8c) the SERS intensity map of the B-H vibrations is shown. This image is a compilation of 15 high-magnification images which were stitched together to produce one very well resolved nanoparticle treated cell surface. The resulting SERS image has been analyzed for features and hot spots, and the amount of nanoparticles can be estimated. The number of nanoparticles on the cell surface is estimated to be around 10^3-10^4, with a large cluster of receptors tethered to 15-20 nanoparticles. The overlaying image in 3.8d) resulting from SEM and SERS maps helps determine the location of the SERS hot spot and clustered nanoparticles. For closer examination, 3.8e) and f) are magnified, where the larger clusters are seen to produce stronger SERS signals due to coupling *via* plasmon resonance (LSPR or SPR) with the nanoparticle plasmons. Control images were also acquired and are displayed in 3.8g) and h). These images were obtained from cells that were treated with the nanoparticle solution, but not the primary anti-EGFR antibody. In

figure 3.8g) the SERS intensity map shows that the cell does not produce noticeable SERS signal on its own, and that targeting the antibody indeed produces strong signals that were observed in 3.8c). In the SEM image 3.8h), the only discernable white features come from precipitated salts. Since it is difficult to differentiate nanoparticles on the cell surface from salt through an SEM image, it is imperative to conduct a SERS intensity map to correctly interpret the white spots.

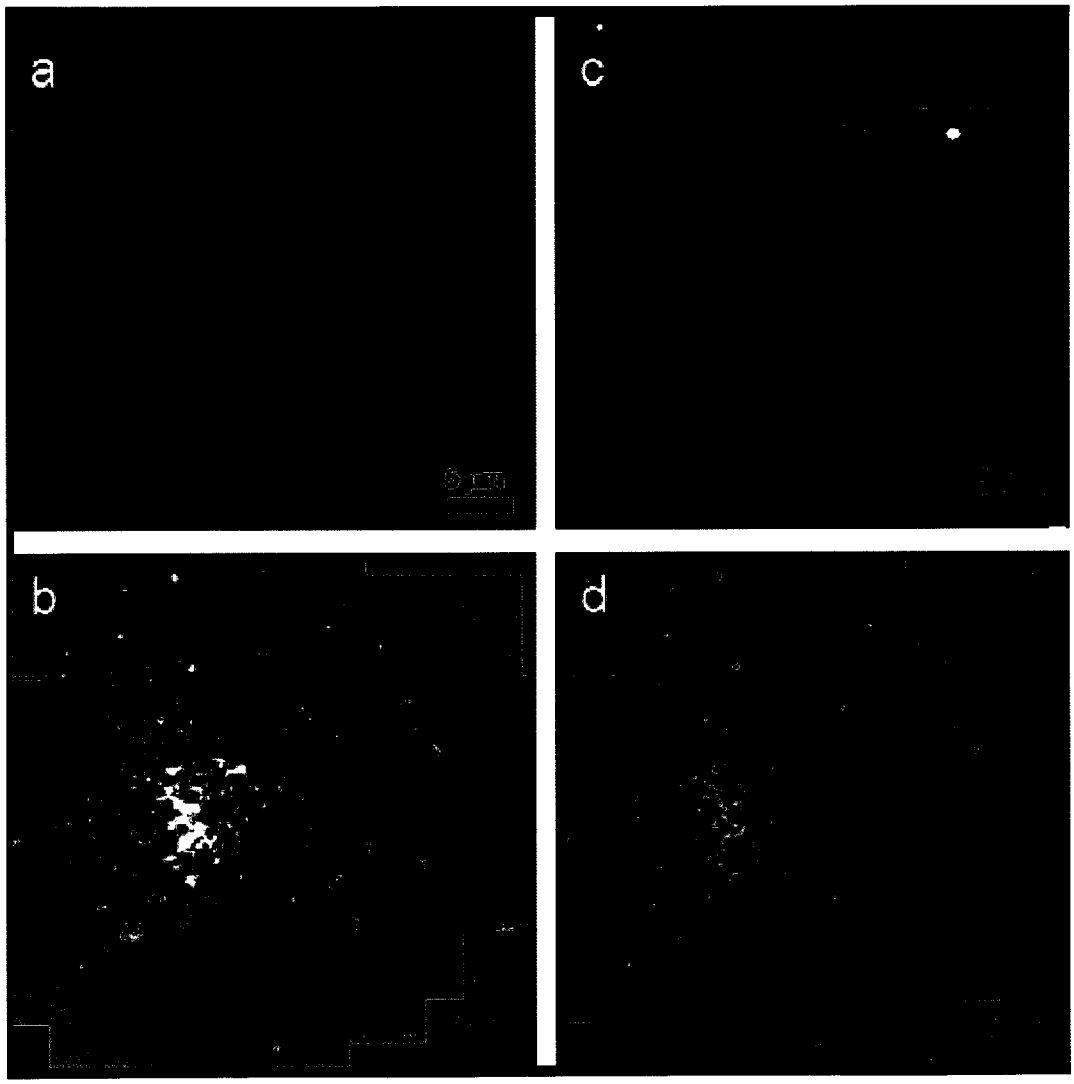

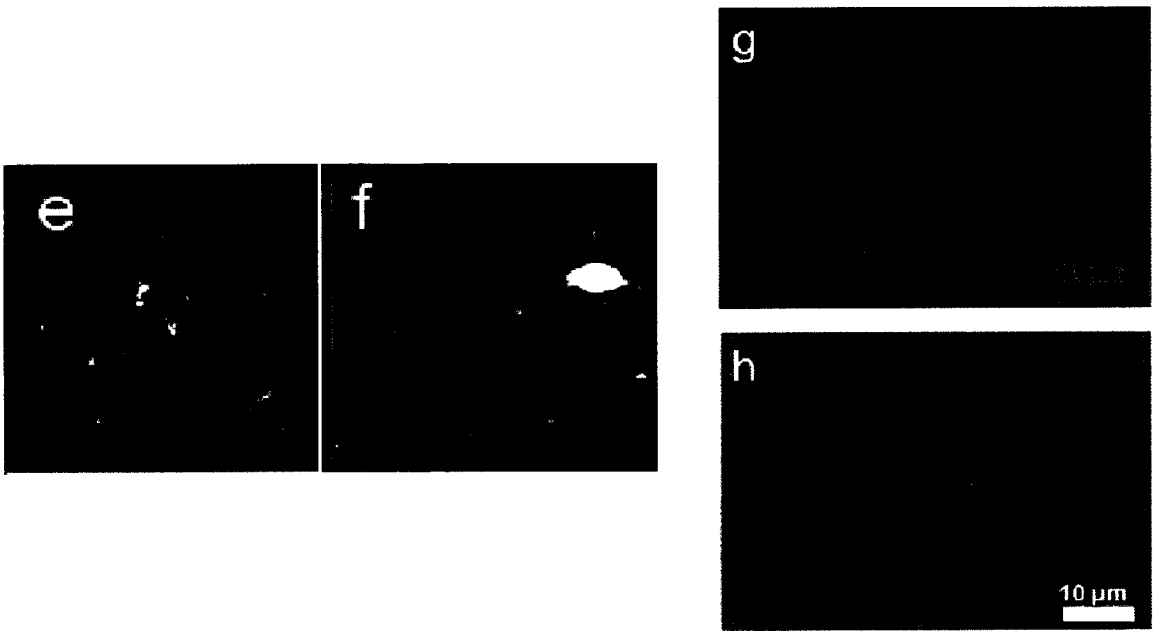

Figure 3.8: Fixed Huh 7 cells, treated with anti-EGFR antibodies and carborane-coated silver nanoparticles, detected through SERS microscopy. 3.8a) The bright field optical image of the cell, 3.8b) High resolution SEM image of the cell, 3.8c) SERS intensity map of the B-H vibrations (2570 cm^{-1}), with hot spots visible, 3.8d) overlay of SERS intensity map c) and the SEM image b) with hot spots highlighted, 3.8e-f) magnification of hot spots from overlaid image, 3.8g) SERS intensity map of control cell, 3.8h) SEM image of control cell, with white spots resulting from salt.

Not only can cells be imaged using these carborane labelled nanoparticles, but the imaging allows for an estimate of the carborane-loading for the cell. This is useful because approximately 10^9 boron atoms are needed per cell to ensure that BNCT can effectively destroy the tumour cell.[79] However, the number of antigen sites on a cell needed for antibody target is roughly 10^6 sites per cell. This means that the BNCT agent

targeting anti-EGFR antibodies must have ~1000 boron atoms per agent to be effective as a therapy. Since the mercapto-carborane possesses 10 boron centres, 100 carboranes would be required per agent in order to reach a therapeutic level. Fortunately the silver nanoparticles have been coated with ~5000 to 10000 mercapto-carboranes, meaning that these are potentially a very potent and effective agent for BNCT. Using the estimate that 10 thiols bind per nm^2 of surface area[80], in a 25 nm nanoparticle with a surface area of ~2000 nm^2, we can determine that a 45% coating of **23** would result in approximately 9000 carboranes covering the silver surface. Regrettably, the number of nanoparticles on the cellular surface is less than the 10^6 antigen sites contained on the cell surface. There are approximately 5000 nanoparticles per cell, since the space required for 10^6 nanoparticles is impossible. Homo-dimers and oligomers are sometimes formed with EGFR receptors, and these can be spaced only 8 nm apart, or less.[81] The 25 nm nanoparticles are not capable of targeting more than one receptor when a dimer occurs, and not all the receptors will be accessible when oligomers are present. If 5000 nanoparticles do bind to the receptor sites, then the loading of boron atoms can be estimated to be ~ 4.5×10^8, a value below therapeutic level. However, this could be ameliorated in a live cell situation, where the receptor-bound nanoparticles may be internalized. This would then allow for additional binding of nanoparticles to the surface as the space is liberated. The total amount of boron calculated to be delivered to the cell is still significant, and with development these agents have potential as therapeutic agents.

Another therapeutic application can be envisioned with the target-specific silver nanoparticles. The silver nanoparticles can also undergo two-photon luminescence. This

feature can be used not only for imaging, but as a heat source as well. With reduced laser power (15 mW average power) luminescent images of the nanoparticles on the cell surface are obtained. However, when the laser power intensity is increased, the nanoparticles absorb energy, which is converted to a localized heat source on the cell surface. This method is already applied as a form of thermal tumour therapy.[82] Here, the power was increased by a factor of 5, and the cells were destroyed by the hot nanoparticles. In figure 3.9, the cells are imaged by two photon luminescence, but by scanning multiple times at an increased power the damage caused by the nanoparticles becomes evident from the black spots. Ultimately, a very large black spot appears after 15 seconds of scanning, which spans over 10μm in diametre. This method is very applicable with the functionalized nanoparticle, since the nanoparticle only binds to the cell when the correct antigen and antibody receptors are in place, as seen with the control experiments from figure 3.8.

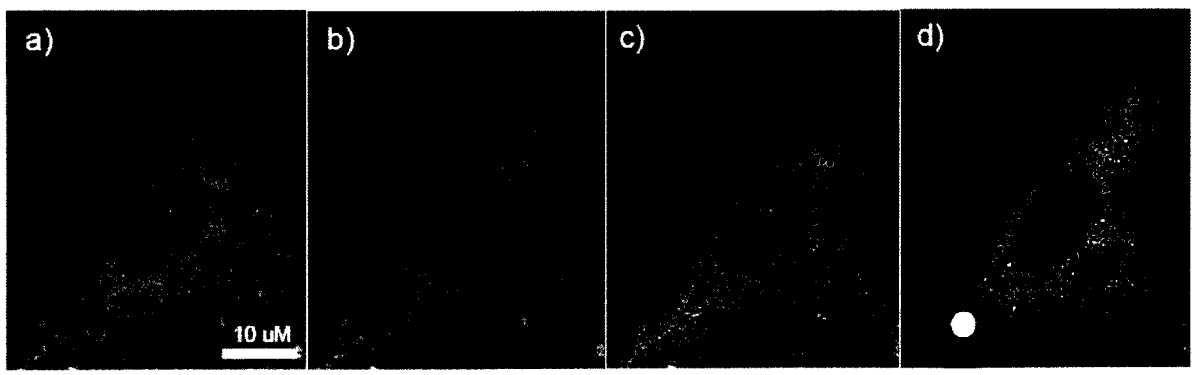

Figure 3.9: Fixed Huh 7.5 cells are treated with the anti-EGFR antibodies, and then with the carborane-coated silver nanoparticles. Using the silver nanoparticles, the cell was imaged through two-photon luminescence 30 times over 15 seconds. In a) t=0 (scan

1) the cell was imaged and the green luminescence resulting from the bound nanoparticle is strong and clearly visible, b) t=5 seconds (scan 11), the first signs of cellular damage from the nanoparticle heat sources are visible with black spots, c) t=10 seconds (scan 21), many black spots are observed from the damage arising from the nanoparticle heat sources, and d) t=15 seconds (scan 30) significant damage is observed, including a very large area over 10μm in diametre.

Here we have seen the application of mercapto-carborane as a distinctive Raman reporter for the use of cellular imaging and possible therapeutic agent. The EGFR antigen was targeted with the anti-EGFR antibody and the functionalized silver nanoparticle through a secondary antibody process, and the silver nanoparticle provided immense SERS signal enhancement through SPR. The cell surface without anti-EGFR treatment did not result in any functionalized nanoparticle binding. The silver nanoparticles also formed localized heat sources which produced apparent cell damage though the use of two-photon luminescence, which demonstrated the potential therapeutic application of this with thermal tumour therapy.

3.3 Experimental

1-mercapto-1,2-dicarba-*closo*-dodecaborane (**23**)

Sodium Hydride (0.48g, 0.02mol) and DME were placed in a Schlenk flask filled with N_2. *O*-carborane (1.45g, 0.01mol) and sulfur (0.641g, 0.02mol) were added. The sulfur turned colour from yellow to green. The mixture was stirred for 7 hours while heated up to 60°C. This solution changed to a dark red colour almost immediately upon heating. After 7 hours, the flask was cooled to 15°C in a cold water bath, and 10 ml of MeOH was added. The dark red solution was decanted, and its solvent was dried *in vacuo*. The resulting red crystalline solid was dissolved in 50 ml H_2O. The aqueous solution was extracted with 50 ml of hexanes. The resulting aqueous layer was acidified with 3ml of 4M HCl, and the products were extracted into 50 ml of benzene. The solvents were removed *in vacuo* to produce 0.693g of yellow solid (39.3% yield). ^1H $\{^{11}B\}$ NMR (500 MHz, $CDCl_3$) δ 3.98 ppm (s, 1H, SH), δ 3.88 ppm (s, 1H, CH), δ 2.50 ppm (s, BH), δ 2.42 ppm (s, BH), δ 2.31 ppm (s, BH), δ 2.23 ppm (s, BH), δ 2.14 ppm (d, BH). Mass Spectrometry actual: 176.17, found: 176.1671.

EG_3SH prepared according to literature procedure: M. Zheng, Z. Li, X. Huang; *Langmuir* **2004**, *20*, 4226

25 nm Silver Nanoparticle Colloid

Prepared from modified Lee and Meisel protocol. A solution of $AgNO_3$ (50.0 ml, 1.0 mM) in 18.2 MΩ deionized water was heated to reflux. A citrate solution (1.0 ml, 51.0mM) was added, and the solution colour slowly turned to gray-yellow. The solution was refluxed for another hour, and then cooled to room temperature. The Ag solution was stored at a temperature of 4°C.

Functionalization of Nanoparticles

The Ag nanoparticles (1ml, ~ 10^{13}/ml) were placed in a glass vial, and DTSP (1μl, 2mM), 1-thio-1,2-dicarba-closo-dodecaborane (6μl, 2mM), and EG_3SH (6μl, 2mM) were added. The solution was stirred for 4 hours, upon which 50μl of the secondary antibody solution (Affinipure goat anti-rabbit IgG (H+L) 2.4 mg/ml from Jackson Immunoresearch) was added. This was mixed by pipetting slowly a few times. The solution was then stored overnight (16 hours) at 4°C. The solution was then warmed to room temperature, and 30μl of bovine serum albumin (BSA) was added. This was mixed with a pipette, and left to stand for 30 minutes. The solution was then transferred to a 1.5 ml Eppendorf micro centrifuge tube and spun at 13.4 k rpm for 20 minutes, which pelleted the particles. The supernatant liquid was removed and the particles were resuspended in 500μl of PBS. The solution was analyzed by UV-Vis and determined to be ~ 1nM. These were stored at 4°C, where they were stable for one month.

Cell Culture samples

Huh 7.5 cells (ATCC, Manassas, VA) were grown in Dulbecco's modified Eagle's medium (Invitrogen, Burlington, ON) supplemented with 10% fetal bovine serum (FBS) (NorthBio, Toronto, ON) under standard culture conditions (37°C, 5% CO_2). These were plated onto silica wafers in a 12 well plate. After 24 hours, the cells were fixed and rinsed with PBS. The anti-EGFR antibody (AB) (EGFR (1005) rabbit polyclonal IgG from Santa Cruz Biotechnology, 0.2 mg/ml, 4μl used per ml PBS) was added, and the cells (+ AB) were then stored in the refrigerator at 4°C for 24 hours. The cells were then rinsed 3 times with PBS, and the 1ml Nanoparticle solution in PBS was used to cover the cells. The cells (+NP) were stored for 24 hours at 4°C. The NP solution was then recovered, and the cells were rinsed again 3 times with PBS, and stored at 4°C in PBS until imaging.

Raman Imaging and Raman Spectroscopy

Raman spectroscopy and microscopy were acquired with a commercial microRaman system (LabRAM HR, Horiba Jobin Yvon) equipped with software controlled XYZ stage and a thermal-electric cooled CCD detector. For most SERS experiments, the samples were excited with 632.8 nm of radiation, at a power density of ~ 10^4 W/cm^2. The incident radiation was coupled into an Olympus BX51 optical microscope and focused to ~ 1 μm diametre spot through a 100X objective. The same objective collects the retro-reflective radiation and guides it to a notch filter, which removes the Rayleigh radiation. For the Raman mapping experiments, a fine set of grid points within an area of interest is defined

in the software, and imaged by rastering the sample under the tightly focused laser beam. At each grid point, a full Raman spectrum was acquired. For Figure 3.8c, the SERS image was generated with a 1 second acquisition time (2 accumulations) with a power density of 10^4 W/cm^2. The multiple accumulations are necessary for the spike removal algorithm to function. Upon completion of mapping, the Raman intensity map of the B-H vibrational mode is regenerated by fitting and removing the associated background for each spectrum in the predefined special grid. The B-H intensity is displayed as a thermal map, as shown in fig 3.8. This is achieved by the Labspec 5.25 software (Horiba Jobin Yvon). The solid mercapto-*p*-carborane Raman spectrum (Figure 3.6) was acquired by 632.8 nm radiation at a power density of ~ 10^5 W/cm^2.

Scanning Electron Microscope

The scanning electron microscope images were obtained on cells plated on Si substrate with a Hitachi S-4700 field emission scanning electron microscope. The samples were imaged with an acceleration voltage of 3KeV, and at a working distance of 12 mm. The high resolution SEM image of the whole cell (Fig 3.8b) was generated from 17 individual high resolution SEM images. Each of these was acquired at 7000X magnification, and the stitching of the images was performed manually with imaging processing software.

Two Photon Luminescence Imaging

The two photon luminescence microscopy system uses a single femtosecond Ti:sapphire oscillator (Spectra Physics Tsunami operating at 80 MHz) as the excitation source (800 nm, 15 mW average power). A modified Olympus Fluoview 300 laser scanning system and IX71 inverted microscope was used to carry out the imaging. A 40X 1.15 Na UAPO water immersion lens with a cover slip collection was used as the objective. Light was directed to the photomultiplier tubes (PMT) with enhanced red sensitivity (Hamamatsu R3896). Two-photon luminescence images were collected on fixed cell samples in PBS in 4.2 cm^2 Lab-Tek Chambers Slide System (NUNC, Rochester, NY). Bright field images were collected simultaneously in order to define the border outlines of cells.

Chapter 4

Improvements and Modifications of the Raman Reporter

4.1 Introduction

The application of the carborane B-H stretch for the purpose of targeted cell imaging has been explored in the previous chapter, where mercapto-carborane as a Raman reporter has been examined. The imaging which resulted from these experiments was very promising, and some improvements have been developed for similar applications.

Some problems which were seen in the last chapter dealt with the functionalized nanoparticle's lack of solubility, as well as the shortfall of total boron loading on the targeted cell surface for BNCT. While the polyethylene glycol linkages (EG_3SH) had to be added with a 1:1 ratio to mercapto-carborane, they covered half of the space available for bonding. If it were possible to integrate a PEG chain into the mercapto-carborane compound, then perhaps more carborane could be loaded onto the nanoparticle without loss in solubility. This chapter explores a carborane compound that was recently reported with the goal of achieving this task. A recent publication by Masateru Ito et al[83] explored the use of long chain hydrophilic groups bound to gold surfaces for NH_2-DNA coupling to produce DNA microarrays. This process, which is used in biosensors and genetic diagnostic devices, uses surface-immobilized single strand probe DNA hybridization with target DNA. Here, they require long chained thiol-capped organic compounds to bind to the gold surface, where the carboxylic acid tail will interact with the NH_2 groups on DNA (Figure 4.1). These long chained organic compounds were measured for the film

thickness. The overall microarray process was monitored by surface plasmon resonance (SPR) imaging. Surprisingly, carborane was a component of one of the long chained compounds as a spacer, and also because of its electron withdrawing properties.

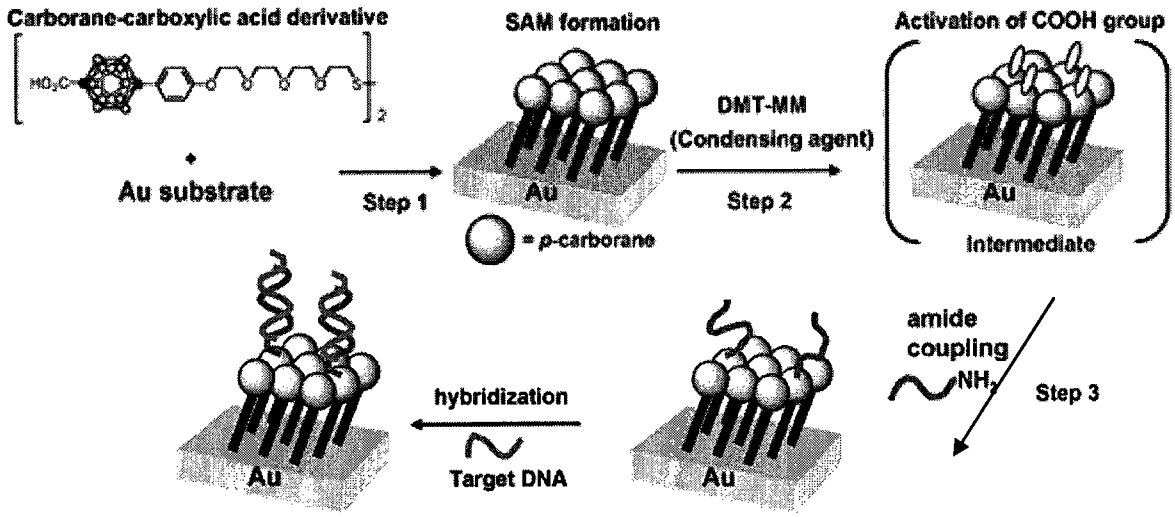

Figure 4.1: Overview of DNA surface coupling reaction, with a carborane PEG derivative.[83]

Two long chained thiols were used in this study, a carborane spacer as well as a benzene spacer (Figure 4.2). The carborane PEG **24** had an overall length of 31Å, where the benzene PEG **25** had an overall length of 20Å. The study determined that the carborane compound was successful in surface coupling reactions with amino functions on DNA. The benzene PEG compound, however, was unable to properly activate the carboxylic acid groups due to dense packing and overall shorter chain lengths. This study was imaged with SPR and had experienced signal enhancement due to the gold nanoparticles.[83]

24) 25)

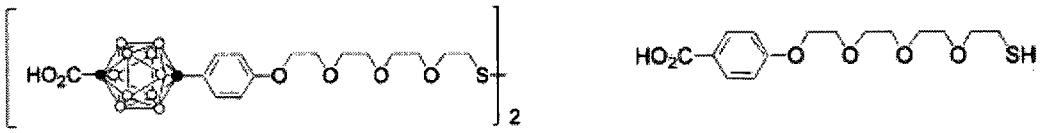

Figure 4.2: Long chained compounds used for NH_2 DNA coupling (**24**) *p*-carborane containing PEG thiol, and (**25**) PEG thiol.[83]

There are many other improvements which can be made to the Raman reporter used on the silver nanoparticle. The use of B-H bond vibrations was chosen because this stretch appears in the spectra, away from naturally occurring cellular signal, as well as the C-H region. There are many other options that could be exploited, some like CMIA were mentioned previously. Another label currently being applied by the Pezacki group is a cyano functional group. The cyano functional group (-C≡N:) has a strong shift in the Raman spectrum at 2230 cm^{-1}, because of the polarizability of the symmetrical CN electron cloud. Cyanides are produced by certain types of fungi, bacteria, and algae, and in fruit seeds and stones. Since C≡N is unique to the cellular environment, and has its own unique Raman shift, it makes for an excellent biomolecular Raman reporter. In addition, C≡N is relatively inert in the chemical conditions for processes like live cell imaging. The Raman reporter was coordinated to silver nanoparticles to image cells with SERS, utilizing the signal enhancement from the silver localized surface plasmons. These functionalized silver nanoparticles were developed to target cellular proteins *in vivo*. Proteins often have very complex spectra and finger print regions, which is why the C≡N functional group was chosen as the vibrational contrast agent. The compound applied as

the Raman reporter also has a terminal hydrazide functional group, which is used to conjugate through ketones to the cell surface proteins.[84]

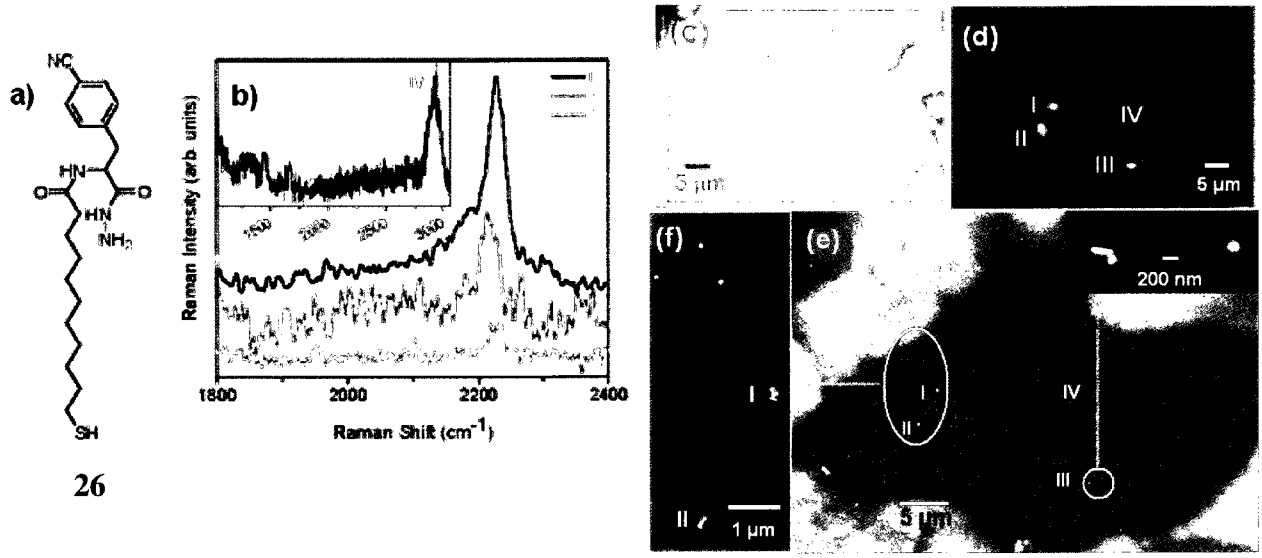

Figure 4.3: a) The Raman reporter (**26**) b) the Raman spectra of CN vibration taken from I, II, and III hotspots, c) optical image of cell, d) Raman intensity map of CN vibrations, e) SEM of the area of d), f) group of nanoparticles expanded from oval on e).[84]

The resulting spectra produced from targeting the cellular surface proteins with the functionalized silver nanoparticles are illustrated in Figure 4.3. The Raman intensity map in d) shows the hot spots numbered I through III. The resulting Raman spectra from these hot spots are illustrated in Figure 4.3b) where the CN vibrational shift is clearly visible. In the inset of b) is the spectrum of IV. Spot IV is the control location, in the same cellular region, but without binding to silver nanoparticles. The shifts in the

spectrum of IV are common for cells, which includes a large band at 2990 cm^{-1} for C-H vibrational shifts. Figure 4.3 e) is the SEM image of the cell, with certain areas highlighted, and f) is the magnification of the SEM oval in e), where I and II hotspots are visible. It is very interesting that the nanoparticles are visible as monomers, dimers, or clusters in the SEM magnification images. It was also concluded from this group that nanoparticle aggregates dramatically increase SERS enhancements, especially as the interstitial gap is on the small scale (~1nm).

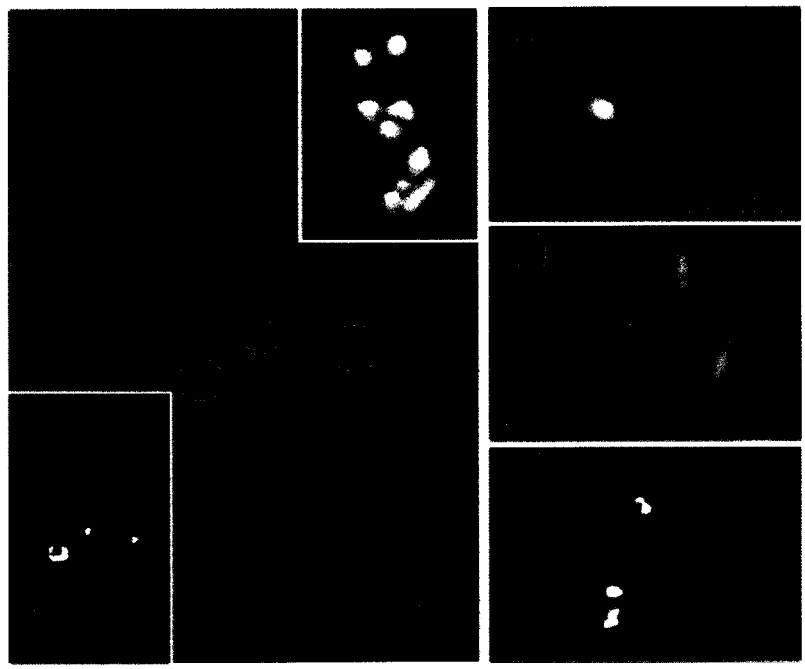

Figure 4.4: a) The SEM image of a cell, with the magnification of nanoparticle clusters in the upper insert, and the Raman intensity map contained in the lower insert, b) laser induced damage from the top blue circle in a), c) laser induced damage where the

nanoparticle aggregates are located, and d) laser induced damage where the nanoparticle dimers are located.[84]

The group also inadvertently examined the nanoparticle-induced photothermal effect on the cells. Since the cells were analysed with intense light beams, some light induced damage may occur. The research group examined cells by SEM before and after the Raman experiments were conducted. The cell membrane did rupture near nanoparticle aggregates, and most of the damage occurred in areas with nanoparticles, as seen in figure 4.4. In Figure 4.4 b-d) there is evidence of cellular damage where the nanoparticles are in close proximity. However, if the laser power density is decreased by a factor of one, damage to the membrane is not observed.[84]

It is evident from the results presented by the Pezacki group that the use of a cyano group as a Raman reporter in a cellular environment performs very well for biological imaging.[84] Along with increasing the solubility and packing possibility of the Raman reporter as discussed with the carborane PEG thiol[83], utilizing different Raman reporters is another method which is examined further in this chapter.

4.2 Discussion

The long chained *p*-carborane PEG compound (**24**) was synthesized based on the methods from Masateru Ito et al. Each compound was analyzed by ^{1}H NMR with comparison to the literature data and not further purified for its use in the following step. Some changes made to the published synthesis are added below, as well as the synthesis of 1,11-dibromotetraethylene glycol. As well, some product characteristics have appeared differently from what is reported. The reaction scheme of the synthesis is shown below in Scheme 4.1 from the Masateru Ito et al publication.[83] The final product exists as a dimer;

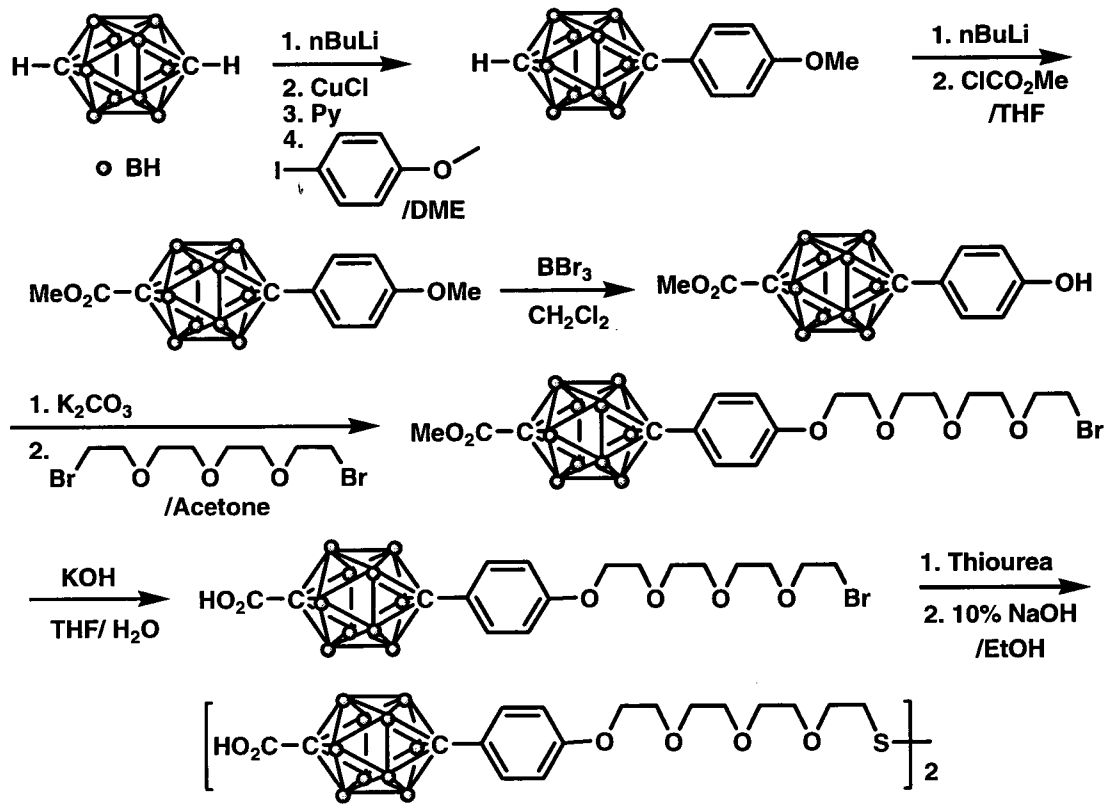

Scheme 4.1: Synthesis of compound **24**

however, it cleaves to produce the monomer upon reaction with the metal center, as described in the literature[83]. Another benefit to the use of **24** as a Raman reporter is the added phenyl functionality next to the carborane moiety. This connection has been known to increase the pseudo-aromaticity of the carborane, and could enhance the B-H vibrational signal mapped by SERS.

The first compound produced in this line of synthetic steps was 1-(4-methoxyphenyl)-1,12-dicarba-*closo*-dodecaborane (**27**). The *para*-carborane isomer was dissolved in dry DME under an inert atmosphere of N_2, and 1.1 equivalents of cold n-butyl lithium were added dropwise into the solution. A white salt precipitate was formed in the solution, and this mixture was stirred for an hour to allow complete mono-deprotonation. Copper (I) chloride was then added to the mixture, which formed a green solution, and was stirred for a further 2 hours. A small quantity of pyridine was then added, and stirred for an additional 30 minutes, before the 4-iodoanisole was added to the mixture. At this point, the Schlenk flask containing the solution under inert atmosphere was sealed, and removed from the glove box. The reaction was continued in the fume hood under a stream of N_2. If the mixture was exposed to air, it formed a brown film on the flask, and no product would result from the reaction. A condenser with streaming N_2 was very quickly added to the Schlenk flask, and the solution was kept under an inert atmosphere. The reaction was heated at reflux for 44 hours at 85°C. The N_2 was streamed through the reaction occasionally, but not so frequently as to evaporate the dry DME contained in the Schlenk. The solution was a red colour once heated at reflux, and eventually became a darker reddish brown colour. Once

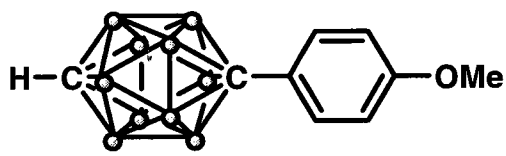

27

the reaction was completed, the solvent was removed *in vacuo* and water was added to the solution, where the products were extracted into diethyl ether. When the combined organic extracts were removed *in vacuo*, an orange solid was obtained. The solid was washed with hexanes and filtered to produce (**27**) as a beige solid with a 26.1 % yield.

The proton NMR was acquired, and the spectrum analyzed for product formation. The spectrum contained two doublets at 7.15 and 6.70 ppm, both of which integrate for 2 protons, and correspond to the protons contained on the phenyl ring. If 4-iodoanisole was still present, the two doublets had neighbouring doublets shifted upfield, or the overlapping doublets created the illusion of triplets or quartets. The methoxy group was represented by a singlet at 3.75 ppm, integrating for 3 protons, meanwhile the remaining CH proton on the carborane appeared at 2.75 ppm. The BH shifts were apparent in the baseline of the spectrum, where the usual line broadening and familiar wave pattern occurred.

The next step in this synthesis was the conversion of the remaining CH carborane proton to a methyl ester group. Product **27** was dried *in vacuo* and dissolved in THF under an inert N_2 atmosphere. Once 1.1 equivalents of cold n-butyl lithium were added dropwise, the solution turned orange in colour and was stirred for 1 hour. The methyl chloroformate reagent was added, and the solution was stirred for an additional 4.5 hours. The solution was removed from the inert atmosphere, and the THF solvent was removed *in vacuo* to produce a gummy orange solid with a yield of 0.122g.

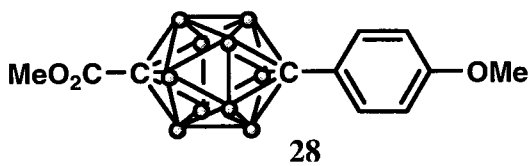

28

Product **28** was analyzed by proton NMR. The two sets of doublets representing the CH protons on the phenyl ring shifted upfield. The shifts were very small, where the doublet at 7.15 ppm was now at 7.09 ppm, and the doublet at 6.70 ppm was now at 6.69 ppm. The methoxy singlet did not change, as expected, however a new singlet appeared at 3.65 ppm, which is indicative of the 3 protons from the new methyl ester terminus. Since the proton NMR spectrum coincided with the published literature, the next step of the synthesis could be performed.

Product **28** was then utilized as a reagent to produce a phenol in place of the methyl phenyl ether. The gummy solid was further dried *in vacuo*, and placed under an inert atmosphere, where it was dissolved in dry dichloromethane. Boron tribromide was added to the solution, and the solution was stored in the freezer at -22°C for a half hour. The solution was periodically removed and stirred at room temperature to ensure adequate mixing, and then replaced in the freezer, as the required 0°C reaction condition from the published synthesis was not possible. This process continued for 4 hours, and then the reaction was placed in the freezer overnight. The solvent was removed *in vacuo* under an inert atmosphere, and then removed into the air, where H_2O was added to the flask. The aqueous solution was extracted with diethyl ether, and the organic extracts were dried with Na_2SO_4. The solvent was removed *in vacuo* to produce a beige solid (**29**) with 91.5% yield.

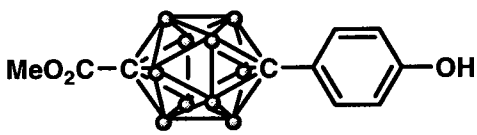

29

In the acquired proton NMR, formation of the product was most clearly indicated by the loss of the singlet of the methoxy function of the starting material.. The apparent peaks were those of the phenyl ring doublets, again shifted minutely upfield, with the

appearance of the methyl ester proton peak at 3.65 ppm. However, the disappearance of the methoxy singlet at 3.75 ppm was indicative of a reaction taking place. The proton from the new alcohol is not discernable; this could be possibly due to an acidic environment.

The polyethylene glycol segment was then added to product **29**, forming product **30**. The beige solid was dissolved in reagent grade acetone under a stream of N_2, and 1,11-dibromotetraethylene glycol was added, as well as Cs_2CO_3. Prior attempts to form the product indicated that K_2CO_3, the reported reagent in the literature, was not an adequate base for the reaction; once Cs_2CO_3 was employed instead the reaction was much more effective. The solution was heated at reflux for 24 hours. Once complete, the solvent was removed *in vacuo* and diethyl ether was added to the flask. The published procedure does mention to extract with diethyl ether, and it is assumed H_2O would be added as well. However, in previous attempts it was discovered that the product was soluble in the aqueous layer, and it was very difficult to recover **30** in good yield. For this synthesis, only diethyl ether was added, and the base formed a green precipitate, where the organic layer was decanted off. The solvent was removed *in vacuo* to form a yellow oil with a yield of 82.7%.

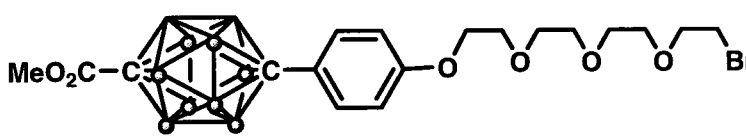

30

The proton NMR was acquired and analyzed for the formation of product **30**. The two sets of doublets for the phenyl ring were still present at similar shifts, as was the singlet for the methyl ester. New peaks appeared in the area of 4.04-4.06 ppm, 3.78-3.82

ppm, and 3.64-3.70 ppm as multiplets accounting for 14 of the 16 glycol protons. The remaining triplet signal, which is associated with the CH_2 neighbouring the terminal bromine, occurs at a shift of 3.45 ppm. Again, in the published experimental the B-H signals are not presented in the data; and these shifts do occur in the baseline between 3.34 and 1.29 ppm.

The next step is to convert the methyl ester group to a pendant carboxylic acid. This step was required by the authors of the published synthesis as a pendant group which would interact with DNA NH_2 groups. Here, the conversion was not required for the purpose of interaction, but the synthetic pathway was followed as a precautionary measure for the final step of the reaction involving NaOH. The yellow oil **30** was dissolved in a THF:H_2O 1:1 mixture and KOH was also added. The reaction was stirred for 6 hours, and the resulting solution was neutralized with dilute HCl. The THF was carefully removed *in vacuo* and H_20 was added to the resulting solution. The products were extracted into ethyl acetate, dried with Mg_2SO_4, and dried *in vacuo* to form an oil (**31**) with 53.9 yield%.

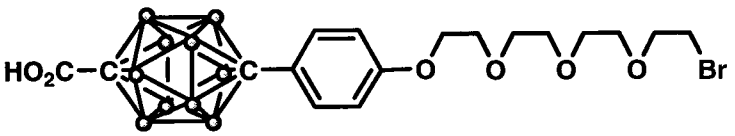

31

The proton NMR spectrum acquired for the oil product showed all of the same peaks for the phenyl and glycol moieties. The methyl ester singlet at 3.65 ppm no longer appears; however, a new peak for the carboxylic acid proton does not appear either. It is possible that the product needed to be acidified to a lower pH for the proton signal to be

detected in the spectrum. The published experimental also does not report a signal for the carboxylic acid proton.

The final step of the synthesis included the exchange of the pendant bromine to a disulfide linked dimeric species. Product **31** was dissolved in ethanol and thiourea was added. The mixture was heated at reflux for 7 hours, at which point a small amount of 10% NaOH was added dropwise and formed a white precipitate in a yellow solution. The reaction was further heated at reflux for another 4 hours. The resulting mixture was neutralized with dilute HCl, and the products were extracted into ethyl acetate. Once the organic extracts were combined and dried with Mg_2SO_4, the solvents were removed *in vacuo* to produce a gray solid (**24**) with 43.6 % yield.

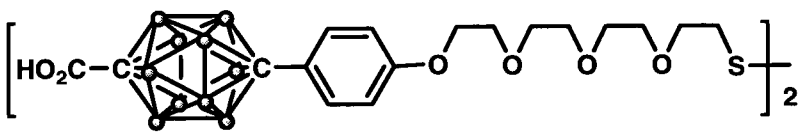

24

Other than the change of shift for 2 protons adjacent to the sulfur, no other protons were shifted in the product. The new CH_2 proton shift was apparent at 2.89 ppm as a triplet; a change from the original triplet that appeared at 3.44 ppm. Although the proton NMR was run in CD_3OD in the published article, this proton NMR was run in $CDCl_3$, as all of the other NMR samples in this synthesis. The resulting peaks corresponded to the published experimental, with only minor shifts. The product was also analyzed by mass spectrometry, where a mass of 943.104 g/mol agreed with the correct formation of **24**. The mass spectrum also contained a peak at 473.029 g/mol, which represents the monomer of **24**.

The synthesis of 1,11-dibromotetraethylene glycol (**32**) was not reported in the same publication. The synthesis of **32** was a modified version of a published experimental, where a tetraethylene glycol was used in the place of a triethylene glycol.[85] Tetraethylene glycol was cooled in a flask in the freezer under an inert atmosphere, and phosphorus tribromide was added dropwise over 30 minutes. If the PBr_3 was added too quickly, it formed a hot exothermic reaction with an orange polymer which could not be removed from the vial once cooled. The mixture, polymer-like at this stage, was removed from the inert atmosphere, and was heated to 50°C over 24 hours. Here the mixture melted to a thick glycol consistency, and was able to be stirred. The mixture was then poured into ice water, and extracted with pyridine. The organic layer was removed *in vacuo* to form a white milky product with 89.5% yield. The proton NMR acquired showed a triplet at 3.80 ppm, a singlet at 3.66 ppm and a second triplet at 3.46 ppm corresponding to the product. No further purifications were conducted to **32**, and **32** was added as a reagent into the synthesis of **30**.

The other improvement to the Raman reporter examined in this chapter is the integration of a cyano group on carborane. This would provide an additional handle useful for SERS and other vibrational analyses. A dimercapto-*p*-carborane was synthesized, and one thiol group was deprotonated and coupled with a CH_2CH_2CN linkage to produce **33**. The synthesis of **33** (dimercapto-p-carborane) was based on similar reactions which were reported by J. Plešek.[78] The *p*-carborane was dissolved in dry diethyl ether under an inert atmosphere, and 2.2 equivalents of cold n-butyl lithium were added. The solution was stirred and the lithio salt precipitated instantly. The mixture was stirred

33

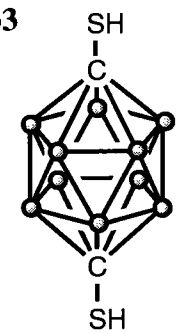

for an hour, at which point sulfur was added to the reaction. The sulfur did not dissolve, and the yellow mixture was stirred overnight. At this point a white precipitate was observed in the place of the yellow sulfur. The reaction was removed from the inert atmosphere, and the solvent was removed *in vacuo*. H_2O was added, dissolving any precipitate, and the solution was acidified to a pH 1.00 by adding dilute HCl dropwise into the solution (creating a new white precipitate). The solution was then extracted with hexanes. The organic extracts were combined, dried with Mg_2SO_4, and removed *in vacuo* to produce a white solid with 64.0 %yield.

The proton NMR spectrum acquired for **33** showed a sharp singlet at 3.07 ppm, representing the two SH protons. The broad multiplet for the BH protons ranged from 3.48-1.50 ppm. Various problems occurred with attempts to form **33**, most notable was the inability to deprotonate both CH protons present on the carborane, even with an excess of n-butyl lithium. The observed result was the appearance of a peak for a CH proton as well as an SH proton in the spectrum. The problem could possibly also stem from the lack of reaction with sulfur, or the disproportionation of the dilithio carborane compound. It is difficult to pinpoint the exact cause of the ineffective dithiol synthesis, although with a few attempts ensuring appropriate excesses of n-butyl lithium and sulfur reagents the product was formed.

The final product **34** was synthesized by adding **33** to dry diethyl ether under an inert atmosphere. The solution was deprotonated carefully with 1 equivalent of cold n-butyl lithium added dropwise, as an excess may produce a mixture of double deprotonated carboranes. The solution was stirred, and a salt precipitated within a few minutes. The solution continued to be stirred for an hour, at which point 1 equivalent of

3-bromopropionitrile was added *via* difference in volume of the syringe, since the volume required was only 38μl. Within a few minutes, the salt disappeared and the solution turned clear. The solution was stirred for 4 hours, at which point it was removed from the inert atmosphere. The solvent was dried *in vacuo* and H_2O was added to the mixture. The solution was acidified to a pH of 1.00 with dilute HCl to ensure protonation, where a white precipitate formed. The product was extracted into diethyl ether, dried over Mg_2SO_4, and the solvent was removed *in vacuo* to produce an oil. The oil was left to crystallize on the bench top, and the result was a mixture of white crystals and oil. These were separated by tilting the round bottom flask to pool the oil separately from the crystals. The white solid was collected and resulted in 29.0 % yield.

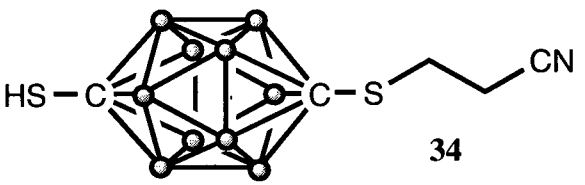

34

The proton NMR spectrum was acquired and analyzed. The spectrum contained two multiplets from 2.84-2.77 ppm and 2.56-2.49 ppm, integrating for 2 protons each, which correspond to the two CH_2 spacer groups. The BH protons are observed by a shallow multiplet ranging from 3.05-1.50 ppm. The SH peak is not discernable in the spectrum. However, the ^{13}C NMR acquired indicates 4 different carbon environments, 117.05 ppm, 75.72 ppm, 31.04 ppm, and 18.05 ppm, which have been assigned to CN, SC-BH, CH_2, and CH_2-CN respectively. From the proton NMR, it is possible that the product formed a disubstituted CH_2CH_2CN carborane since the remaining SH peak is missing. Nevertheless, from the carbon NMR the 4 distinct carbon signals indicate that

the final product was formed. The formation of product was confirmed by mass spectrometry with a peak at 261.2.

4.3 Experimentals

General

Reagents and solvents used were obtained form Aldrich Chemicals, with the exception of the carborane isomers, which were purchased from Katchem Ltd. NMR spectra were recorded on a Bruker Avance 300 MHz, or 500 MHz NMR spectrometer using the residual protons of the deuterated solvent for reference. Raman spectroscopy was acquired with a microRaman system (LabRAM HR, Horiba Jobin Yvon). The Raman spectrums were acquired by 632.8 nm irradiation at a power density of ~ 10^5 W/cm^2. Mass Spectroscopy Electron Ionization was acquired with a Kratos Concept Tandem Mass Spectrometer by the University of Ottawa Mass Spectroscopy Center.

1-(4-methoxyphenyl)-1,12-dicarba-*closo*-dodecaborane (**27**)

To a solution of *p*-carborane (0.290g, 2.0 mmol) in 15 ml dry DME under N_2 atmosphere, was added cold 1.6M n-butyl lithium (1.5ml, 2.2mmol), which quickly formed a white salt precipitate. The reaction mixture was stirred for 1 hour, after which dry copper (I) chloride (0.22g, 2.2mmol) was added. The solution was stirred for 2 hours, and 1.2 ml of dry pyridine was added and stirred for 30 minutes. Once 4-iodoanisole (0.44g, 2.0mmol) was added to the mixture, the Schlenk vessel was sealed and removed from the glove box. The mixture was then heated at reflux to a temperature of 85°C for 44 hours under a stream of N_2. The refluxed solution started red, and finished a reddish brown colour. The

solvent was removed *in vacuo*, and H_2O was added to the mixture. The solution was extracted with diethyl ether (4x20 ml), and the organic layers were combined, dried with Na_2SO_4, and evaporated *in vacuo* forming a pale orange solid. This was washed with hexanes and filtered to obtain the beige product (0.173g) with 26.1% yield. ^{1}H NMR (300 MHz, $CDCl_3$) δ 7.15 ppm (d, 2H, CH), δ 6.70 ppm (d, 2H, CH), δ 3.75 (s, 3H, OCH_3), δ 2.75 (s, 1H, CH), δ 3.44-1.55 (m, 10H, BH).

1-(4-methoxyphenyl)-12-formic acid methyl ester-1,12-dicarba-*closo*-dodecaborane (**28**)

To a solution of **27** (0.100g, 0.4mmol) in 15 ml dry THF under N_2 atmosphere was added cold 1.6M n-butyl lithium (0.28 ml, 0.44mmol), upon which the solution turned orange in colour. This mixture was stirred for 1 hour, and methyl chloroformate (0.034ml, 0.44mmol) was added. The solution was stirred for 4.5 hours, and subsequently removed from the inert atmosphere. The solvent was removed *in vacuo* and resulted in a sticky orange mass, with a yield of 0.122g. ^{1}H NMR (300 MHz, $CDCl_3$) δ 7.09 ppm (d, 2H, CH), δ 6.69 ppm (d, 2H, CH), δ 3.74 ppm (s, 3H, CH_3), δ 3.65 ppm (s, 3H, CH_3), δ 3.52-1.41 ppm (m, 10H, BH).

1-(4-hydroxyphenyl)-12-formic acid methyl ester-1,12-dicarba-*closo*-dodecaborane (**29**)

To a solution of **28** (0.122g, 0.40 mmol) in dry dichloromethane under N_2 atmosphere was added BBr_3 (0.07ml, 0.75 mmol). The solution was stirred for 3 hours and the temperature was alternated from room temperature to -22°C, as the temperature could not

be cooled to 0°C in the inert atmosphere. The solution was then stored in the freezer overnight at -22°C. Afterwards, the solvent was removed *in vacuo* and H_2O was added. The product was extracted into diethyl ether (3 x 15ml), dried with Na_2SO_4, and recovered once the solvent had been dried *in vacuo*. The beige solid (0.104g) was collected with a yield of 91.5%. ^1H NMR (300 MHz, $CDCl_3$) δ 7.04 ppm (d, 2H, CH), δ 6.61 ppm (d, 2H, CH), δ 3.65 ppm (s, 3H, CH_3), δ 3.25-1.35 ppm (m, 10H, BH).

1-(12-formic acid methyl ester-1,12-dicarba-*closo*-dodecaborane)-4-(1-bromo)-tetraethyleneglycol (**30**)

To a solution of **29** (0.240g, 0.82mmol) in acetone under N_2 was added 1,11-dibromotetraethyleneglycol (0.422g, 1.2mmol) and Cs_2CO_3 (0.863g, 2.45mmol). The solution was heated at reflux for 24 hours. The solvent was removed *in vacuo* and diethyl ether was added (note, do not extract with H_2O as product soluble in aqueous layer). Caesium carbonate formed a green precipitate, and the organic layer was decanted off of it. The solvent was removed *in vacuo* and the product was collected as yellow oil (0.362g, 82.7% yield). ^1H NMR (300 MHz, $CDCl_3$) δ 7.07 ppm (d, 2H, CH), δ 6.69 ppm (d, 2H, CH), δ 4.04-4.06 ppm (m, 2H, CH_2), δ 3.78- 3.82 ppm (m, 4H, CH_2), δ 3.65 ppm (s, 3H, CH_3), δ 3.64-3.70 (m, 8H, CH_2), δ 3.45 ppm (t, 2H, CH_2), δ 3.34-1.29 ppm (m, 10H, BH).

1-(12-formic acid-1,12-dicarba-*closo*-dodecaborane)-4-(1-bromo)-tetraethyleneglycol (**31**)

To a solution of **30** (0.362g, 0.679mmol) in 30 ml THF:H_2O mixed solution (1:1) was added potassium hydroxide (0.190g, 3.40 mmol). The reaction was stirred for 6 hours, and then neutralized with dilute HCl (0.06 ml of 12M). The THF was removed *in vacuo*, and the residue was dissolved 5 ml additional H_2O and extracted with ethyl acetate (3x 15ml). The organic layers were combined and dried with Mg_2SO_4. The solvent was removed *in vacuo* to produce an oil (0.190g, 53.9% yield). ^{1}H NMR (300 MHz, $CDCl_3$) δ 7.07 ppm (d, 2H, CH), δ 6.69 ppm (d, 2H, CH), δ 4.04-4.06 ppm (m, 2H, CH_2), δ 3.77-3.82 ppm (m, 4H, CH_2), δ 3.65-3.70 ppm (m, 8H, CH_2), δ 3.44 ppm (t, 2H, CH_2), δ 3.30-1.25 ppm (m, 10H, BH).

12-(4-(12-formic acid-1,12-dicarba-*closo*-dodecaborane)-phenoxy)-tetraethyleneglycol-disulfide (**24**)

To a solution of **31** (0.190g, 0.37mmol) in 15 ml ethanol was added thiourea (0.139g, 1.83mmol). The reaction was heated at reflux at 105°C for 7 hours, after which NaOH (0.7ml of a 10% solution) was added dropwise. This formed a white precipitate in the yellow solution. The reaction was again heated at reflux for 4 hours. The solution was then neutralized with dilute HCl. The solution was then extracted with ethyl acetate (3 x 15ml). The organic layers were combined and dried *in vacuo* to produce gray solid with 43.6 % yield. ^{1}H NMR (300 MHz, $CDCl_3$) δ 7.14 ppm (d, 2H), δ 6.69 ppm (d, 2H),

δ 4.04-4.06 ppm (m, 2H), δ 3.73-3.76 (m, 4H), δ 3.60-3.68 ppm (m, 8H), δ 2.89 ppm (t, 2H). Mass Spectroscopy: actual 943.20; found: 943.104.

1,11-dibromotetraethyleneglycol (**32**)

Tetraethylene glycol (5.83g, 30 mmol) was placed into a vial under N_2 atmosphere and PBr_3 (8.12g, 30 mmol) was added drop wise over 30 minutes. The polymer-like mixture was removed from the inert atmosphere and heated at 50°C for 24 hours (upon which the mixture melted into a glycol like consistency). The mixture was poured into ice water, and the organic layer was extracted with pyridine (containing water). The solvents were removed with heat *in vacuo* and resulted in a milky white product (8.6g, 89.5% yield). ^1H NMR (500 MHz, $CDCl_3$) δ 3.80 ppm (t, 4H, CH_2), δ 3.66 ppm (s, 8H, CH_2), δ 3.46 ppm (t, 4H, CH_2).

1,12-dimercapto-1,12-dicarba-*closo*-dodecaborane (**33**)

To a solution of *p*-carborane (0.104g, 0.72mmol) in 8 ml of dry diethyl ether under an inert atmosphere was added 1.6 M cold n-butyl lithium (0.99ml, 1.58mmol). The solution was stirred for 1 hour. Sulfur (0.051g, 1.58mmol) was then added to the reaction, and the solution was stirred overnight, where it turned from a yellow to a white salt solution. The solvent was then removed *in vacuo* and 5ml H_2O was added. The solution was then acidified to pH 1.00 with dilute HCl (~4M), where white precipitate was formed. The solution was extracted with hexanes (3x20 ml), and the organic layers were combined

and dried with Mg_2SO_4. The hexanes were then removed *in vacuo* to result in a white solid (0.096g, 64.0% yield). ^1H NMR (300 MHz, $CDCl_3$) δ 3.48-1.50 ppm (m, 10H, BH), δ 3.07 ppm (s, 2H, SH).

3-(12-mercapto-1-thio-1,12-dicarba-*closo*-dodecaborane)propanenitrile (**34**)

To a solution of **33** (0.096g, 0.461mmol) in dry diethyl ether under an inert atmosphere was added cold 1.6 M n-butyl lithium (0.30 ml, 0.46 mmol). The solution precipitated into a white salt and was stirred for 1 hour. 3-bromopropionitrile (0.038ml, 0.461 mmol) was added to the solution, and within a few minutes the solution turned clear. The solution was stirred for 4 hours, upon which it was removed from the inert atmosphere. The solvent was removed *in vacuo* and H_2O was added to the vial. The solution was acidified to a pH of 1.00 with dilute HCl (~ 4M) and a white solid precipitated. The aqueous solution was extracted with diethyl ether (3x20 ml), and the organic extracts were combined and dried with Mg_2SO_4. The solvent was removed *in vacuo* to result in crystalline solid with oil residue, which was separated by gravity to result in white crystals (35mg, 29.0% yield). ^1H NMR (500 MHz, $CDCl_3$) δ 2.84-2.77 ppm (m, 2H, CH_2), δ 2.56-2.49 ppm (m, 2H, CH_2), δ 3.05-1.50 (m, 10H, BH); ^{13}C {^1H} NMR (500 MHz, $CDCl_3$) δ 117.05 ppm (CN), δ 75.72 ppm (C-BH), δ 31.04 ppm (CH_2), δ 18.05 ppm (CH_2-CN). Mass Spectroscopy actual: 261.16, found: 261.1648.

Conclusions and Future Directions

In this thesis a short overview of imaging, spectroscopy, and nanoparticles was presented for reference on background information in Chapter 1. In Chapter 2, we explored the uses of carborane in medicine, and discussed the synthesis of functionalized carboranes to use for unique spectroscopic vibrations. The synthesis of a variety of ligand groups on various carborane isomers resulted in a few pathway conclusions. Carborane disproportionates, and so careful lithiation is required for a mono-functionalized carborane product. Also, various conditions are used for different isomers, and *o*-carborane can be deprotonated easier than the *m*-carborane, which is concurrent with various proton acidity tables. The *o*-carborane forms a salt at room temperature once lithiated; however, the *m*-carborane isomer only forms a salt at ~ -10°C. To note, the *p*-carborane reactions in Chapter 3 also form insoluble salts at room temperature. The library of compounds synthesized in low to moderate yields was useful in examining isomer reactivity and spectroscopic information.

Chapter 3 examined the use of a mercapto-*p*-carborane on a silver nanoparticle selectively targeting anti-EGFR antibody on malignant cell surfaces. The silver nanoparticles were functionalized with a carborane thiol stock solution, triethylene glycol thiol, DTSP, and the appropriate secondary antibody. In the absence of the polyethylene glycol, the functionalized nanoparticles aggregate and precipitate in water. However, if the ratio of PEG:carborane is changed, the resulting BH vibrations weaken. The resulting Raman microscopy images illustrated the strong enhancement due to the functionalized silver nanoparticles. The SEM and SERS vibrational maps were overlaid, and

nanoparticle hotspots were identified, with one area having 15-20 nanoparticles tethered. The control samples were treated with the nanoparticle solution, but not with the required anti-EGFR antibody. As a result, the functionalized nanoparticles were not observed, and did not react with any other cell surface receptor. The calculated amount of carborane deposited is just shy of the required quantity for successful BNCT processes. However, this may change depending on live cell reactions. Two-photon luminescence was preformed on cells treated with the same nanoparticle solution and anti-EGFR antibodies. These images were very clear, and upon energy intensification, the cells had significant thermal cellular destruction caused by the hot silver nanoparticles. Control cells did not exhibit any cellular destruction. Research is further warranted on both the live cell receptor targeting for BNCT, and the two-photon luminescence as a form of thermal therapy, since these showed very promising results.

Finally, in Chapter 4 further improvements were made to the mercapto-*p*-carborane for uses in anti-EGFR antibody targeted SERS imaging. A long chain PEG-containing compound was synthesized in order to improve the nanoparticle solubility, and to increase the concentration of carborane contained on the nanoparticle for BNCT use. A new compound was synthesized, X, for an additional CN Raman handle. Since cyano functionalized silver nanoparticles have been used for similar research, it is expected that the BH and CN groups on compound X will provide useful identifying information. In the future, these compounds need to be added to silver nanoparticles and undergo tests with anti-EGFR antibody treated malignant cells for imaging. Hopefully the SERS results will inspire alternate therapeutic methods in the medical sector.

References

[1] M. Abramowitz, Fluorescence Microscopy: the essentials; Olympus America Inc, 1993, pp 5.

[2] D. Wöhrle, A.D. Pomogaĭlo, Metal Complexes and Metals in Macromolecules; Wiley-VCH Verlag GmbH & Co; Weinheim, 2003, pp 35.

[3] http://en.wikipedia.org/wiki/Infrared_spectroscopy

[4] http://carbon.cudenver.edu/public/chemistry/classes/chem4538/raman.htm

[5] E. Smith, G. Dent, Modern Raman Spectroscopy: A practical Approach; John Wiley and Sons; West Sussex England, 2005, pp 113.

[6] J. A Creighton, D. G Eadon; *J. Chem. Soc., Faraday Trans*, **1991**, *87*, 3881

[7] http://www.d3diagnostics.com/en/10256.aspx

[8] J.R. Lombardi, R. L. Birke; *Acc. Chem. Res.*, **2009**, *42* (6), 734

[9] A. Campion, P. Kambhampati; *Chem. Soc. Rev.*, **1998**, *27*, 241

[10] K. Kneipp, M. Moskovits, H. Kneipp; Surface Enhanced Raman Scattering: Physics and Application; Springer-Verlag, Berlin, 2006, pp 162

[11] P. K. Aravind, A. Nitzan, H. Metiu; *Surf. Sci.*, **1981**, *110*, 189; P. K. Aravind, H. Metiu; *J. Phys. Chem.* **1982**, *86*, 5076; P. K. Aravind, H. Metiu; *Surf. Sci.*, **1983**, *124*, 506; N. Liver, A. Nitzan, J. I. Gersten; *Chem. Phys. Lett.*, **1984**, *111*, 449

[12] H. X. Xu, M. Käll; *Chem. Phys. Chem.*, **2003**, *4*, 1001; H. Xu, J. Aizpurua, M. Käll, P. Apell; *Phys. Rev. B*, **2000**, 62, 4318

[13] Nie, S; Emory, S.R; *Science*, **1997**, *275*, 1102

[14] C. J. Murphy, A. M. Gole, J. W. Stone, P. N. Sisco, A. M. Alkilany, E. C. Goldsmith, S. C. Baxter; *Acc. Chem. Res.*, **2008**, *41* (12), 1721

[15] P. K. Jain, X. Huang, I. H. El-Sayed, M. A. El-Sayed; *Acc. Chem. Res.*, **2008**, *41* (12), 1578

[16]http://www.naturessunshine.ca/ca/products/catalog/product/default.aspx?stocknum=4950

[17] J. R Morones, J. L Elechiguerra, A. Camacho, K. Holt, J.B. Koun, J.T. Ramirez, M.J. Yacaman; *Nanotechnology*, **2005**, *16*, 2346

[18] P. K Jain, X. Huang, I. H. El-Sayed, M. A. El-Sayed; *Plasmonics*, **2007**, *2*, 107

[19] a) U.Kreibig, M.Vollmer; Optical Properties of Metal Clusters; Springer, Berlin, 1995, pp 25; S. Link, M. A. El-Sayed, *Annu. Rev. Phys. Chem.*, **2003**, *54*, 331; b) S.Eustis, M. A. El-Sayed; *Chem. Soc. Rev.*, **2006**, *35*, 209

[20] a) C. J. Murphy, T. K. Sau, A. M. Gole, C. J. Orendorff, J. Gao, L. Gou, S. E. Hunyadi, T. J. Li; *Phys. Chem. B*, **2005**, *109*, 13857; b) S. Link, M. B. Mohamed, M. A. El-Sayed; *J. Phys. Chem. B*, **1999**, *103*, 3073; c) Erratum; *J. Phys. Chem. B*, **2005**, *109*, 10531

[21] P. K. Jain, K. S. Lee, I. H. El-Sayed, M. A. El-Sayed; *J. Phys. Chem. B*, **2006**, *110*, 7238

[22] C. Sönnichsen, B. M. Reinhard, J. Liphardt, A. P. A. Alivisatos; *Nat. Biotechnol.*, **2005**, *23*, 741

[23] A. P. Alivisatos; *Nat. Biotechnol.*, **2004**, *22*, 47

[24] a) S. J. Oldenburg, R. D. Averitt, S. L. Westcott, N. J. Halas; *Chem. Phys. Lett.*, **1998**, *28*, 243; b) P. K. Jain, M. A. El-Sayed; *Nano Lett.*, **2007**, *7*, 2854

[25] a) W.R. Chen, R.L. Adams, R. Carubelli, R.E. Nordquist; *Cancer Lett.*, **1997**, *115*, 25; b) M. Castren-Persons, T. Schroder, O.J. Ramo, P. Puolakkainen, E. Lehtonen; *Lasers Surg. Med.*, **1991**, *11*, 595; c) S.M. Waldow, P.R. Morrison, L.I. Grossweiner; *Lasers Surg. Med.*, **1988**, *8*, 510; d) C. M. Philipp, E. Rohde, H. P. Berlien; *Semin. Surg. Oncol.*, **1995**, *11*, 290

[26] F. A. Jolesz, K. Hynynen; *Cancer J.*, **2002**, 8 (1), S100–S12.

[27] a) G. S. Gazelle, S. N. Goldberg, L. Solbiati, T. Livraghi; *Radiology*, **2000**, *217*, 633; b) A. N. Mirza, B. D. Fornage, N. Sneige, H. M. Kuerer, L. A. Newman, F. C. Ames, S. E. Singletary; *Cancer J.* **2001**, *7*, 95; c) T. Seki, M. Wakabayashi, T. Nakagawa, M. Imamura, T. Tamai, A. Nishimura, et al; *Cancer* **1999**, *85*, 1694

[28] D. P. O'Neal, L. R. Hirsch, N. J. Halas, J. D. Payne, J. L. West; *Cancer Letters*, **2004**, *209*, 171

[29] a) T. L. Heying, J. W. Ager, Jr, S. L. Clark, D. J. Mangold, H. L. Goldstein, M. Hillman, R. J. Polak, J. W. Szymanski; *Inorg. Chem.* **1963**, *2*, 1089; b) M. M. Fein, J. Bobinski, N. Mayes, N. Schwartz, M. S. Cohen; *Inorg. Chem.* **1963**, *2*, 1111

[30] a) L. I. Zakharkin, V. I. Stanko, V. A. Brattsev, Y. A. Chapovskii, Y.T. Struchov; *Izv. Akad. Nauk. SSSR. Ser. Khim.* **1963**, *2*, 2069; b) L. I. Zakharkin, V. I. Stanko, V .A. Brattsev, Y. A. Chapovskii, O. Y. Okhlobystin; *Izv. Akad. Nauk. SSSR. Ser. Khim.* **1963**, *12*, 2238

[31] C. A. Brown, M. L. McKee; *J. Molec. Mod.*,**2006**, *12*(5), 653

[32] a) R. N. Grimes; *Carboranes*; Academic Press, New York, 1970; b) L. Gmelin, *Gmelin Handbook of Inorganic Chemistry*, 8th ed.; Springer-Verlag, Berlin, 1988, 4

[33] http://www.sigmaaldrich.com/MSDS/MSDS/DisplayMSDSPage.do

[34] a) A. N. Kashin; K. P. Butin; V. I. Stanko; I. P. Beletskaya; *Izv. Akad. Nauk. SSSR. Ser. Khim.*, **1969**, *9*, 1917; b) L. A. Leites; *Chem. Rev.* **1992**, *92*, 279

[35] J. Plešek, S. Heřmánek; *Chem. Ind.*, **1977**, *9*, 360

[36] L. I. Zakharkin, I. V. Pisareva, K. R. Bikkineev; *Izv. Akad. Nauk. SSSR. Ser. Khim.*, **1977**, *26*, 641.

[37] a) V. I. Bregadze, V. T. Kampel, N. N. Godovikov; *J. Organomet. Chem.* **1976**, *112*, 249; b) V. I. Bregadze, A. Y. Usiatinsky, N. N. Godovikov; *J. Organomet. Chem.*, **1985**, *292*, 75

[38] D. L. Rabenstein, T. T. Nakashima; *Anal. Chem.*, **1979**, *51*, 1465A

[39] http://u-of-o-nmr-facility.blogspot.com/2008/04/1-h-nmr-with-11-b-decoupling.html

[40] G. L. Locher, A. J. Roentgenol; *Radium Ther.*, **1936**, *36*, 1

[41] a) P. A. Zahl, F. S. Cooper, J. R. Dunning; *Proc. Natl. Acad. Sci.* USA, **1940**, *26*, 589; b) W. H. Sweet, M. Javid; *Trans. Am. Neurol. Assoc.*, **1951**, *76*, 60; c) A. D. Conger, N. H. Giles, Jr.; *Genetics,* **1950**, *35,* 397; d) M. Javid, G. L. Brownell, W. H. Sweet; *J. Clin. Invest.*, **1952**, *31*, 604; e) H. J. Taylor; *Proc. R. Soc. London A*, **1935**, *147,* 873

[42] a) R. G. Fairchild, V. P. Bond; *Int. J. Radiat. Oncol. Biol. Phys.*, **1985**, *11*, 831; b) R. G. Zamenhof, A. M. Kalend, W. D. Bloomer; *J. Natl. Cancer Inst.*, **1992**, *84*, 1290; c) M. F. Hawthorne; *Mol. Med. Today*, **1998**, *4*, 174

[43]http://nanomed.missouri.edu/index.php?cat=research&groups=&person=&researchpaper=BNCT&

[44] J. F.Valliant, K. J. Guenther, A. S. King, P. P. Schaffer, O. O. Sogbein, K. A. Stephenson; *Coord. Chem. Rev*, **2002**, *232*, 173

[45] a) P. H. Seeberger, W. C. Haase; *Chem. Rev.*, **2000**, *100*, 4349; b) S. Nishimura; *Curr. Opin. Chem. Biol.* **2001**, *5*, 325; c) P. Sears, C. H. Wong; *Science*, **2001**, *291*, 2344

[46] a) L.F. Tietze, U. Bothe; *Chem. Eur. J.*, 1998, *4*, 1179; b) L. F. Tietze, U. Bothe, U. Griesbach, M. Nakaichi, T. Hasegawa, H. Nakamura, Y. Yamamoto; *Bioorg. Med. Chem.*, **2001**, *9*, 1747

[47] T. Hartman, J. Carlsson; *Radiother. Oncol.*, **1994**, *31*, 61

[48] L. Gedda, H. Ghaneolhosseini, P. Nilsson, K. Nyholm, J. Pettersson, S. Sjöberg, J. Carlsson; *Anti-Cancer Drug Des.* **2000**, *15*, 277

[49] a) A. H. Soloway, W. Tjarks, A. Barnum, F. G. Rong, R. F. Barth, I. M. Codogni, J. G. Wilson; *Chem. Rev.*, **1998**, *98*, 1515; b) K. Shelly, D. A. Feakes, M. F. Hawthorne, P. G. Schmidt, T. A. Krisch, W. F. Bauer; *Proc. Natl. Acad. Sci. USA,* **1992**, *89*, 9039; c) D. A. Feakes, K. Shelly, M. F. Hawthorne; *Proc. Natl. Acad. Sci. USA,* **1995**, *92*, 1367; d) A. M. Moraes, M. H. A. Santana, R. G. Carbonell; *J. Microencaps.*, **1999**, *16*, 647; e) W. Chen, S. C. Mehta, D. R. Lu; *Adv. Drug Deliv. Rev,.* **1997**, *26*, 231; f) N. Bergstrand, E. Bohl, J. Carlsson, K. Edwards, H. Ghaneolhosseini, L. Gedda, M. Johnsson, M. Silvander, S. Sjöberg; *Contemp. Boron Chem. Spec. Publ. R. Soc. Chem.*, **2000**, *253*, 131; g) D. A. Feakes, J. K. Spinler, F. R. Harris; *Tetrahedron*, **1999**, *55*, 11177

[50] K. Y. Rho, Y. J. Cho, C. M. Yoon; *Tetrahedron Lett.*, **1999**, *40*, 4821

[51] D. M. Adams, W. Ji, R. F. Barth, W. Tjarks; *Anticancer Res.*, **2000**, *20*, 3395

[52] W. Karnbrock, H.J. Musiol, L. Moroder; *Tetrahedron*, **1995**, *51*, 1187

[53] A.T. Tatham, H. Nakamura, E.C. Wiener, Y. Yamamoto; *Mag. Res. Med.*, **1999**, *42*, 32

[54] P. Gund; *Prog. Mol. Subcell. Biol,.* **1977**, *5*, 117

[55] I. H. Hall, A. Elkins, W. J. Powell, S. Karthikeyan, A. Sood, B. F. Spielvogel; *Anticancer Res.*, **1998,** *18*, 2617

[56] a)Y. Endo, T. Iijima, Y. Yamakoshi, H. Fukusawa, C. Miyaura, M. Inada, A. Kubo, A. Itai; *Chem. Biol.* 2001, *8*, 341; b)Y. Endo, T. Iijima, Y. Yamakoshi, A. Kubo, A. Itai; *Bioorg. Med. Chem. Lett.*, **1999**, *9*, 3313; c) T. Meyers, R. Koop, E. von Angerer, H. Schonenberger, E. A. Holler; *J. Cancer Res. Clin. Oncol.*, **1994**, *120*, 359

[57] a)Y. Endo, T. Yoshimi, Y. Yamakoshi; *Chem. Pharm. Bull.*, **2000**, *48*, 312; b)Y. Endo, T. Iijima, Y. Yamakoshi, M. Yamaguchi, H. Fukasawa, K. Shudo; *J. Med. Chem,* **1999**,

42, 1501; c)Y. Endo, T. Yoshimi, T. Iijima, Y. Yamakoshi, Bioorg; *Med. Chem. Lett.*, **1999**, *9*, 3387; d) L. F. Tietze, U. Bothe, U. Griesbach, M. Nakaichi, T. Hasegawa, H. Nakamura, Y. Yamamoto; *Chem. Biol. Chem.*, **2001**, *2*, 326; e)H. P. C. Hogenkamp, D. A. Collins, D. Live, L. M. Benson, S. Naylor; *Nucl. Med. Biol.*, **2000**, *27,* 89; f) R. McCague, G. Leclercq, N. Legros, J. Goodman, G. M. Blackburn, M. Jarman, A. P. Foster; *J. Med. Chem.*, **1989**, *32* , 2527; g) R. McCague, I. B. Parr, B. P. Haynes; *Biochem. Pharmacol.*, **1990**, *40*, 2277; h) J.A. Katzenellenbogen, K. E. Carlson, B. S. Katzenellenbogen; *J. Steroid Biochem.*, **1985**, *22*, 589; i) S. R. D. Johnston, S. Riddler, B. P. Haynes, R. Ahern, I. E. Smith, M. Jarman, M. Dowsett, *Br. J. Cancer*, **1997**, *75*, 804

[58] J. F. Valliant, P. Morel, P. Schaffer, J. H. Kaldis; *Inorg. Chem.*, **2002**, *41*, 628

[59] a) M. Argentini, D. F. D. Santos, R. Weinreich, H. J. Hansen; *Inorg. Chem.* **1998**, *37*, 6018; b)D. F. dos Santos, M. Argentini, R. Weinreich, H. J. Hansen; *Helv. Chim. Acta,* **2000**, *83*, 2926

[60] G. W. Kabalka, M. Davis, P. Bendel; *Mag. Res. Med.*, **1988**, *8*, 231

[61] A.T. Tatham, H. Nakamura, E.C. Wiener, Y. Yamamoto; *Mag. Res. Med.*, **1999**, *42*, 32.

[62] a) J. C. Yanch, S. Shortkroff, R. E. Shefer, S. Johnson, E. Binello, D. Gierga, A. G. Jones, G. Young, C. Vivieros, A. Davison, C. Sledge; *Med. Phys.*, **1999**, *26*, 364; b) D. P. Gierga, J. C. Yanch, R. E. Shefer; *Med. Phys.*, **2000**, *27*, 203

[63] R. A. Watson-Clark, M. L. Banquerigo, K. Shelly, M. F. Hawthorne, E. Brahn; *Proc. Natl. Acad. Sci. USA*, **1998**, *95,* 2531

[64] J. F. Valliant, P. Schaffer, J. F. Britten, A. Davison, A. G. Jones, J. C. Yanch, *Tetrahedron Lett.*, **2000**, 41, 1355

[65] R. A. Tripp, R. A. Dluhy, Y. Zhao; *Nano Today*, **2008**, *3* (3-4), 31

[66] T. J. Lynch, D. W. Bell, R. Sordella, S. Gurubhagavatula, R. A. Okimoto, B. W. Brannigan, P. L. Harris, S. M. Haserlat, J. G. Supko, F. G. Haluska, D. N. Louis, D. C. Christiani, J. Settleman, D. A. Haber; *N. Engl. J. Med.*, **2004**, *350* (21), 2129

[67] H. S. Wiley; *J. Cell. Physiol.*, **1988**, *107*, 801

[68] R. Zidovetzki, Y. Yarden, J. Schlessinger, T. M. Jovin; *Proc. Natl. Acad. Sci. U.S.A.*, **1981**, *78*, 6981

[69] www.tarceva.com

[70] a) J. Yguerabide, E. E. Yguerabide; *J. Cell. Biochem.*, **2001**, 84(37), 71; b) P. Alivisatos; *Nat. Biotechnol.*, **2004**, *22*(1), 47; c) K. Aslan, J. R. Lakowicz, C. D. Geddes; *Curr. Opin. Chem. Biol.*, **2005**, *9*(5), 538

[71] C. J. Barnes, R. Kumar; *Cancer Treat Res.*, **2004**, *119*, 1

[72] a) P. Mathevet, L. Frappart, and W. Hittelman; *Gynecologie, Obstetrique & Fertilité*, **2000**, 28(1), 44; b)D. M. Shin, I. B. Gimenez, J. S. Lee, K. Nishioka, M. J. Wargovich, S. Thacher, R. Lotan, T. J. Slaga, and W. K. Hong; *Cancer Res.***1990**, *50*(8), 2505; c)D. S. Lidke, P. Nagy, R. Heintzmann, D. J. Arndt-Jovin, J. N. Post, H. E. Grecco, E. A. Jares-Erijman, and T. M. Jovin; *Nat. Biotechnol.*, **2004**, *22*(2), 198

[73] J. Aaron, N. Nitin, K. Travis, S. Kumar, T. Collier, S. Y. Park, M. José-Yacamán, L. Coghlan, M. Follen, R. Richards-Kortum, K. Sokolov; *J. of Biomed Opt.*, **2007**, *12*(3), 034007

[74] X. Huang, I. H. El-Sayed, W. Qian, M. A. El-Sayed; *Nano Lett.*, **2007**, *7* (6), 1591

[75] Friedrich, M. G; Kirste, V. U; Zhu, J; Gennis, R. B; Knoll, W; Naumann, R. L. C; *J. Phys. Chem B*, **2008**, *112*, 3193

[76] http://www.secondary-antibody.com/

[77] N. J. Durr, T. Larson, D. K. Smith, B. A. Korgel, K. Sokolov, A. Ben-Yakar; *Nano Lett.*, **2007**, *7*(4), 941

[78] a) J. Plešek , S. Heřmánek; *Col. Czech. Chem. Com.*, **1981**, *46*, 687; b) J. Plešek , Z. Janoušek, S. Heřmánek; *Col. Czech. Chem. Com.*, **1980**, *45*, 1775

[79] E. I. Tolpin, G. R. Wellum, F. C. Dohan, Jr., P. L. Kornblith, R. G. Zamenhof; *Oncology*, **1975**, *32*, 223

[80] Q. Hu, L. L. Tay, M. Noestheden, J.P. Pezacki; *J. Am. Chem. Soc.*, **2007**, *129*, 14

[81] X. Huang, I. H. El-Sayed, W. Qian, M. A. El-Sayed; *Nano. Lett.*, **2007**, *7*, 1591

[82]A. M. Gobin, J. J. Moon, J. L. West; *Int. J. Nanomed,*. **2008**, *3*, 351

[83] M. Ito, F. Nakamura, A. Baba, K. Tamada, H. Ushijima, K. H. A. Lau, A. Manna, W. Knoll; *J. Phys. Chem. C*, **2007**, *111*, 11653

[84] Q. Hu, L. Tay, M. Noestheden, J. P. Pezacki; *J. Am. Chem. Soc.*, **2007**, *129*, 14

[85] J. F. W. Keana, Y. Wu, G. Wu; *J. Org. Chem.*, **1987**, *52* (12), 2571

Appendix A

X-ray Crystallography Experimental and Data

Crystals of $[C_5H_{16}B_{10}O_2]$ (**21**) were grown from pentane/hexane.A single coloreless needle suitable for X-ray diffraction measurements was mounted on a glass fibre. Unit cell measurements and intensity data collections were performed on a Bruker-AXS SMART 1 k CCD diffractometer using graphite monochromatized Mo K_α radiation (λ = 0.71073 Å). The data reduction included a correction for Lorentz and polarization effects, with an applied multi-scan absorption correction (SADABS). The crystal data and refinement parameters for $[C_5H_{16}B_{10}O_2]$ are listed in Table 2.2. Interatomic distances and angles are listed in Table 2.1. The reflection data were consistent with a triclinic system; P-1.

The crystal structure was solved and refined using the SHELXTL program suite. Direct methods yielded all non-hydrogen atoms which were refined with anisotropic thermal parameters. All hydrogen atom positions were either located from the difference Fourier maps or were calculated geometrically and were riding on their respective carbon atoms. The largest residual electron density peak (0.288 e/Å^3) was associated with the B11 atom. Full-matrix least-squares refinement on F^2 gave R_1 = 0.1132 and wR_2 = 0.2773 at convergence. The high R value may be due to multiple twinning of the crystal. The data was checked for twinning using the programs 'rotax' and 'cell now'. The twinning could not be resolved using the twin laws derived from either program, however, cell now gave evidence of multiple twinning; of the 775 reflections read into the program, only 443 reflections (51%) could be assigned to the given unit cell domain (1) while the remaining 332 reflections were assigned to several other unit cell domains.

Table 2.2: Crystal data and structure refinement for **21**

Identification code	08035
Empirical formula	C5 H16 B10 O2
Formula weight	216.28

Temperature	202(2) K	
Wavelength	0.71073 Å	
Crystal system	Triclinic	
Space group	P-1	
Unit cell dimensions	a = 10.379(3) Å	α= 103.577(4)°.
	b = 10.410(3) Å	β= 101.227(4)°.
	c = 12.667(4) Å	γ = 91.806(4)°.
Volume	1300.6(7) $Å^3$	
Z	4	
Density (calculated)	1.104 Mg/m^3	
Absorption coefficient	0.061 mm^{-1}	
F(000)	448	
Crystal size	0.50 x 0.08 x 0.04 mm^3	
Theta range for data collection	2.29 to 25.02°.	
Index ranges	-12<=h<=12, -12<=k<=12, -15<=l<=15	
Reflections collected	10320	
Independent reflections	4444 [R(int) = 0.1357]	
Completeness to theta = 25.02°	96.8 %	
Absorption correction	Semi-empirical from equivalents	
Max. and min. transmission	0.9976 and 0.9701	
Refinement method	Full-matrix least-squares on F^2	
Data / restraints / parameters	4444 / 1 / 315	
Goodness-of-fit on F^2	1.013	
Final R indices [I>2sigma(I)]	R1 = 0.1132, wR2 = 0.2773	
R indices (all data)	R1 = 0.1927, wR2 = 0.3288	
Largest diff. peak and hole	0.288 and -0.247 $e.Å^{-3}$	